Quarterly Technical Report

Solid State Research
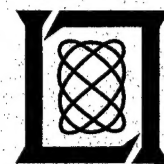
19990618 189

1999:1

Lincoln Laboratory

MASSACHUSETTS INSTITUTE OF TECHNOLOGY

LEXINGTON, MASSACHUSETTS

This technical report has been reviewed and is approved for publication.

FOR THE COMMANDER

Gary Tutungian
Administrative Contracting Officer
Contracted Support Management

MASSACHUSETTS INSTITUTE OF TECHNOLOGY
LINCOLN LABORATORY

SOLID STATE RESEARCH

QUARTERLY TECHNICAL REPORT

1 NOVEMBER 1998 — 31 JANUARY 1999

ISSUED 11 JUNE 1999

LEXINGTON   MASSACHUSETTS

ABSTRACT

This report covers in detail the research work of the Solid State Division at Lincoln Laboratory for the period 1 November 1998 through 31 January 1999. The topics covered are Quantum Electronics, Electro-optical Materials and Devices, Submicrometer Technology, Biosensor and Molecular Technologies, Microelectronics, Analog Device Technology, and Advanced Silicon Technology. Funding is provided by several DoD organizations—including the Air Force, Army, BMDO, DARPA, Navy, NSA, and OSD—and also by the DOE, NASA, and NIST.

TABLE OF CONTENTS

LIST OF ILLUSTRATIONS

LIST OF ILLUSTRATIONS (Continued)

LIST OF ILLUSTRATIONS (Continued)

LIST OF TABLES

INTRODUCTION

1. QUANTUM ELECTRONICS

The output of a passively Q-switched microchip laser has been used to pump standard single-mode silica fiber, resulting in a compact, extremely broadband source of near-diffraction-limited radiation in the visible and near-infrared portions of the spectrum. A variety of nonlinear effects including stimulated Raman scattering, self phase modulation, cross phase modulation, and four-wave mixing are responsible for the generation of the supercontinuum.

2. ELECTRO-OPTICAL MATERIALS AND DEVICES

Improved accuracy has been achieved in mass-transported GaP and GaAs microlenses by orienting the mesa preforms away from the cleave directions. Weighted Strehl ratios greater than 80% have been obtained.

3. SUBMICROMETER TECHNOLOGY

Transient absorption in fused silica optical materials under 193-nm wavelength irradiation has been studied. The magnitude of this effect is shown to be large enough to introduce significant exposure dose errors in lithographic systems.

Advanced photolithography has been used to fabricate interdigitated microelectrode arrays that pass steady-state limiting currents of up to 230 nA/μM analyte—2.5 times more than the most sensitive interdigitated array built to date—and exhibit response times of ~5 ms. This performance results from the small interelectrode gap and the large active area of the device (4 mm^2), a combination enabled by 193-nm photolithography.

4. BIOSENSOR AND MOLECULAR TECHNOLOGIES

Feasibility has been demonstrated for a bioelectronic sensor designed to detect bacterial and viral pathogens, which uses live cells derived from the immune system. The rationale and development of an alternative detecting cell, the fibroblast, are described.

5. MICROELECTRONICS

A compact blooming-control structure for back-illuminated charge-coupled device (CCD) imagers has been developed for which the fabrication requires only a single mask step followed by two ion implants. Measurements on a test imager show suppression of blooming for pixel overloads in excess of 10^6.

6.   ANALOG DEVICE TECHNOLOGY

A prototype superconductive programmable binary-analog matched filter for a 2-Gchip/s direct-sequence spread-spectrum modem has been operated for the first time and has performed correlation using a pseudonoise code pattern. Although problems prevented operation at the design speed, the results demonstrate that all components of the filter are fully functional.

7.   ADVANCED SILICON TECHNOLOGY

Left-right critical dimension asymmetries observed with chromeless phase-edge masks, resulting from mask- or stepper-related effects, have been found to be related to coma aberration which can be aggravated by the presence of lens tilt effects. Pitch asymmetries have also been studied and found to be related to mask errors which can be significantly enhanced for pitch values approaching the Rayleigh resolution limit.

REPORTS ON SOLID STATE RESEARCH

1 NOVEMBER 1998 THROUGH 31 JANUARY 1999

PUBLICATIONS

Planar Integration of a Resonant-Tunneling Diode with pHEMT Using a Novel Proton Implantation Technique	C. L. Chen L. J. Mahoney S. D. Calawa R. H. Mathews K. M. Molvar J. P. Sage P. A. Maki T. C. L. G. Sollner	*IEEE Electron Device Lett.* **19**, 478 (1998)
Cooled Yb:YAG for High-Power Solid State Lasers	T. Y. Fan T. Crow[*] B. Hoden[*] F. Way[*]	*Proc. SPIE* **3381**, 200 (1998)
Theory and Experimental Results of New Diamond Surface-Emission Cathode	M. W. Geis N. Efremow, Jr. K. E. Krohn J. C. Twichell T. M. Lyszczarz	*Nature* **393**, 431 (1998)
PbTe/Te Superlattice Structures with Enhanced Thermoelectric Figures of Merit	T. C. Harman D. L. Spears M. P. Walsh	*J. Electron. Mater.* **28**, L1 (1999)
Excimer-Laser-Induced Degradation of Fused Silica and Calcium Fluoride for 193-nm Lithographic Applications	V. Liberman M. Rothschild J. H. C. Sedlacek R. S. Uttaro A. Grenville A. K. Bates[*] C. Van Peski[*]	*Opt. Lett.* **24**, 58 (1999)

---

[*]Author not at Lincoln Laboratory.

Testing of Optical Materials for 193-nm Applications	V. Liberman M. Rothschild J. H. C. Sedlacek R. S. Uttaro A. Grenville[*] A. K. Bates[*] C. Van Peski[*]	*Proc. SPIE* **3427**, 411 (1998)
Microchip Lasers	J. J. Zayhowski	*Opt. Mater.* **11**, 255 (1999)
Passively *Q*-Switched Microchip Lasers and Applications	J. J. Zayhowski	*Rev. Laser Eng.* **26**, 841 (1998)

ACCEPTED FOR PUBLICATION

The Photomixer Transceiver	S. Verghese K. A. McIntosh S. D. Calawa W. F. DiNatale E. K. Duerr[*] L. H. Mahoney	*Proc. SPIE*
Characterization of Recombination Processes in Doubly-Capped Quaternary Thin Films for Antimonide-Based Thermophotovoltaic Devices	C. A. Wang S. Saroop[*] J. Borreg[*] R. Gutman[*] G. Charache[*]	*J. Appl. Phys.*

PRESENTATIONS[†]

Geiger-Mode Avalanche Photodiode Arrays Integrated with CMOS Timing Circuits	B. F. Aull	Meeting of the Boston Chapter of the IEEE Electron Devices Society, Lexington, Massachusetts, 3 November 1998

---

[*]Author not at Lincoln Laboratory.

[†]Titles of presentations are listed for information only. No copies are available for distribution.

Hydride Vapor Phase Epitaxy Growth of GaN Films	R. J. Molnar	9th Seoul International Symposium on the Physics of Semiconductors and Applications, Seoul, Korea, 6-7 November 1998
Origin of Exchange Field Reductions in Diluted Magnetic Garnets	G. F. Dionne	43rd Magnetism and Magnetic Materials Conference, Miami, Florida, 9-12 November 1998
Magnetic Design for Low-Field Tunability of Microwave Ferrite Resonators	G. F. Dionne D. E. Oates	
Microchip Lasers	J. J. Zayhowski	Lincoln Laboratory Technical Seminar Series, University of Michigan, Ann Arbor, Michigan, 10 November 1998
Critical Issues in 157-nm Lithography	T. M. Bloomstein M. Rothschild R. R. Kunz D. E. Hardy R. B. Goodman S. T. Palmacci	3rd International Workshop on Charged Particles, Waikoloa, Hawaii, 10-14 November 1998
Resonant-Tunneling-Diode Digital Filters	T. C. L. G. Sollner J. P. Sage C-L. Chen P. A. Maki M. A. Hollis R. Mathews	1998 Advanced Heterostructure Workshop, Kamuela, Hawaii, 29 November– 4 December 1998
Investigation of the Enhanced 3D Thermoelectric Figure of Merit in Novel PbTe Based Superlattices	T. C. Harman T. Koga[*] X. Sun[*] S. B. Cronin[*] M. S. Dresselhaus[*]	1998 Fall Meeting of the Materials Research Society, Boston, Massachusetts, 30 November– 4 December 1998

[*]Author not at Lincoln Laboratory.

High-Power, High-Efficiency, Quasi-CW 4-μm Sb-Based Laser	H. Q. Le G. W. Turner S. Buchter J. L. Daneu C. H. Lin[*] S. S. Pei[*]	
Hydride Vapor Phase Epitaxy Growth of GaN Films	R. J. Molnar	1998 Fall Meeting of the Materials Research Society, Boston, Massachusetts, 30 November– 4 December 1998
Limiting Phase Separation in Epitaxial GaInAsSb	C. A. Wang S. Ransom D. C. Oakley H. K. Choi	
Comparison of the Microwave Frequency Power Dependence of Surface Resistance of Unpatterned and Patterned YBCO Thin Films	H. Xin D. E. Oates A. C. Anderson M. S. Dresselhaus[*] G. Dresselhaus[*]	
The Use of Proton Bombardment to Reduce the Effects of Photo-generated Free Carriers in Passive InGaAsP/InP Waveguide Devices	J. P. Donnelly S. H. Groves K. L. Hall R. R. Thoen[*] E. P. Ippen[*]	Lasers and Electro-Optics Society Annual Meeting, Orlando, Florida, 1-4 December 1998
Tunable 1.3-μm Fiber Ring Laser Employing a Tapered Diode Amplifier	R. C. Williamson G. E. Betts J. P. Donnelly S. H. Groves J. N. Walpole F. J. O'Donnell R. J. Bailey	

[*]Author not at Lincoln Laboratory.

ORGANIZATION

SOLID STATE DIVISION

D. C. Shaver, *Head*
R. W. Ralston, *Associate Head*
N. L. DeMeo, Jr., *Assistant*
Z. J. Lemnios, *Senior Staff*

J. W. Caunt, *Assistant Staff*
K. J. Challberg, *Administrative Staff*
J. D. Pendergast, *Administrative Staff*

SUBMICROMETER TECHNOLOGY

M. Rothschild, *Leader*
T. M. Lyszczarz, *Assistant Leader*
T. H. Fedynyshyn, *Senior Staff*
R. R. Kunz, *Senior Staff*

Astolfi, D. K.	Goodman, R. B.
Bloomstein, T. M.	Krohn, K. E.
Craig, D. M.	Liberman, V.
DiNatale, W. F.	Maki, P. A.
Doran, S. P.	Palmacci, S. T.
Efremow, N. N., Jr.	Palmateer, S. C.
Forte, A. R.	Sedlacek, J. H. C.
Geis, M. W.	Uttaro, R. S.

QUANTUM ELECTRONICS

A. Sanchez-Rubio, *Leader*
T. Y. Fan, *Assistant Leader*
T. H. Jeys, *Senior Staff*

Aggarwal, R. L.	DiCecca, S.
Buchter, S. C.	Dill, C., III
Cook, C. C.	O'Brien, P. W.
Daneu, J. L.	Ochoa, J. R.
Daneu, V.	Zayhowski, J. J.

ELECTRO-OPTICAL MATERIALS AND DEVICES

D. L. Spears, *Leader*
J. C. Twichell, *Assistant Leader*
G. W. Turner, *Assistant Leader*
H. K. Choi, *Senior Staff*
R. C. Williamson, *Senior Staff*

Bailey, R. J.	Liau, Z. L.	Oakley, D. C.
Betts, G. E.	Lightfoot, A.	O'Donnell, F. J.
Calawa, A. R.*	Mahoney, L. J.	Poillucci, R. J.
Calawa, D. R.	Manfra, M. J.	Reeder, R. E.
Calawa, S. D.	McIntosh, K. A.	Taylor, P. J.
Connors, M. K.	Missaggia, L. J.	Verghese, S.
Donnelly, J. P.	Molnar, R. J.	Walpole, J. N.
Goodhue, W. D.	Mull, D. E.	Wang, C. A.
Harman, T. C.	Napoleone, A.	Wasserman, J. L.
Harris, C. T.	Nitishin, P. M.	

*Part Time

xxi

BIOSENSOR AND MOLECULAR TECHNOLOGIES

M. A. Hollis, *Leader*

Graves, C. A.	Petrovick, M. S.
Mathews, R. H.	Rider, T. H.
Parameswaran, L.	Young, A. M.

ANALOG DEVICE TECHNOLOGY

T. C. L. G. Sollner, *Leader*
L. M. Johnson, *Assistant Leader*
A. C. Anderson, *Senior Staff*

Ala'ilima, T. F.	Murphy, P. G.
Berggren, K. K.	Oates, D. E.
Boisvert, R. R.	Paul, S. A.
Feld, D. A.	Sage, J. P.
Fitch, G. L.	Santiago, D. D.
Holtham, J. H.	Seaver, M. M.
Lyons, W. G.	Slattery, R. L.
Macedo, E. M., Jr.	Whittington, R. H.

MICROELECTRONICS

B. B. Kosicki, *Leader*
R. K. Reich, *Assistant Leader*
B. E. Burke, *Senior Staff*

Aull, B. F.	Johnson, K. F.
Cooper, M. J.	Lind, T. A.
Daniels, P. J.	Loomis, A. H.
Doherty, C. L., Jr.	McGonagle, W. H.
Dolat, V. S.	O'Mara, D. M.
Donahue, T. C.	Percival, K. A.
Felton, B. J.	Young, D. J.
Gregory, J. A.	

ADVANCED SILICON TECHNOLOGY

C. L. Keast, *Leader*
P. W. Wyatt, *Associate Leader*

Adourian, A.	Newcomb, K. L.
Berger, R.	Rabe, S.
Bozler, C. O.	Rathman, D. D.
Burns, J. A.	Reinold, J. H., Jr.
Chen, C. K.	Sexton, S. V.
Chen, C. L.	Soares, A. M.
Davis, P. V.	Suntharalingam, V.
D'Onofrio, R. P.	Tyrrell, B. M.
Frankel, R. S.	Yost, D.-R.
Fritze, M.	Young, G. R.
Knecht, J. M.	

1. QUANTUM ELECTRONICS

1.1 MICROCHIP-LASER-BASED SUPERCONTINUUM GENERATION

High-brightness light sources with broad spectral bandwidth have many important applications including white-light interferometry, three-dimensional imaging, and differential-absorption lidar. A traditional approach to supercontinuum generation (>200-nm bandwidth) has been the propagation of intense ultrashort pulses (<100 ps) from modelocked lasers through condensed matter. Spectral broadening of the input pulse can result from various nonlinear processes such as stimulated Raman scattering (SRS), self phase modulation (SPM), cross phase modulation (XPM), and four-wave mixing (FWM). An alternative, in the nanosecond pulse regime, has been to employ a polychromatic phase-matching geometry in an optical parametric oscillator. However, the laser systems in both of these approaches are inherently complex and not very robust. We have employed a variation of the first technique using a passively Q-switched microchip laser [1] emitting at either 1064 or 532 nm as the pump source and standard single-mode fiber as the nonlinear media [2]. The result is an extremely compact and robust system with near-diffraction-limited output over very wide spectral ranges.

The output of the passively Q-switched laser consists of 10-μJ pulses, ~400 ps in length, at 1064 nm. The pulses are diffraction limited, which allows efficient coupling to the optical fiber. Intensities of >10 GW/cm^2 are readily achievable in the fiber core. A diagram of the experimental setup is shown in Figure 1-1. As the pulse propagates down the 100-m length of fiber, several different nonlinear interactions occur. Figure 1-2(a) is a spectrum of the 1064-nm-pumped fiber output. The output energy of 2 μJ corresponds to a net conversion efficiency of 20%. Within the first few meters of the fiber, the first Stokes SRS pulse is generated. It is spectrally broadened with respect to the pump as a result of the rather large Raman gain bandwidth (~40 THz) in silica fibers. As its intensity grows, the threshold for the second-order SRS pulse is reached, with the first-order pulse acting as the pump. This pulse is broadened further, and the process continues to higher-order SRS pulses. As the wavelength crosses into the region of negative group-velocity dispersion (~1300 nm), new processes begin to dominate. Modulation instability breaks up the pulses into
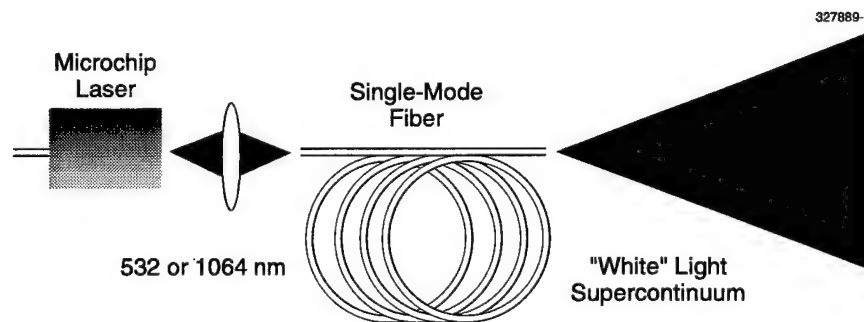
Figure 1-1. Fiber-Raman continuum generation.

1

329762-1

10 μJ, 1.064-μm Pump
2-μJ Total Output

Intensity

Wavelength (μm)

0.75   0.95   1.15   1.35   1.55   1.75   1.95   2.15   2.35

5 μJ, 532-nm Pump
0.5-μJ Total Output

Intensity

Wavelength (μm)

500   600   700   800   900   1000
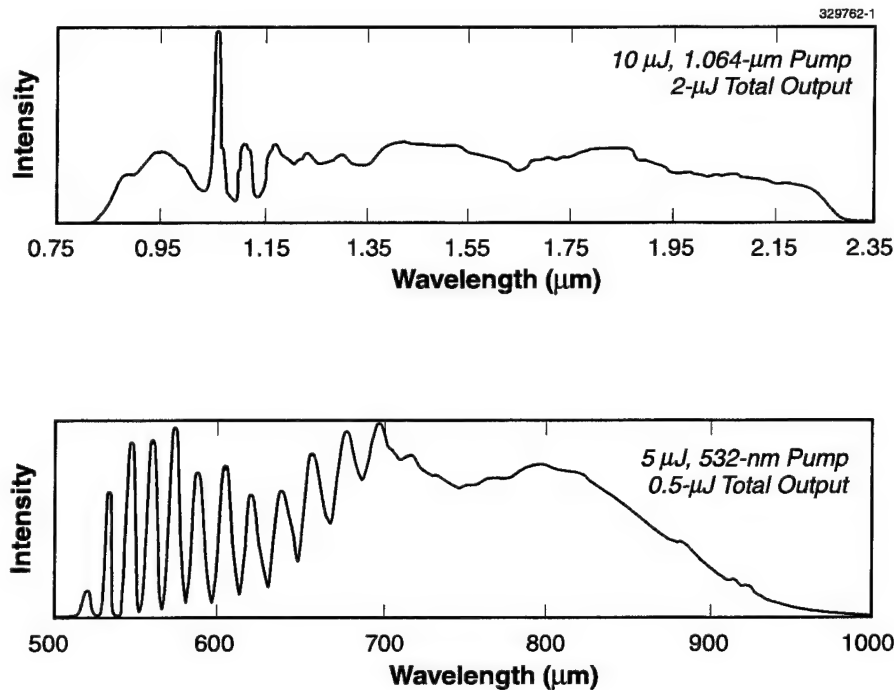
Figure 1-2. Output spectra of ir- and green-pumped fibers.

trains of shorter pulses. As these pulses travel down the fiber, they experience soliton compression. When the pulse duration becomes sufficiently short (10's of picoseconds or less), SPM and XPM become important. Because the time derivative of the phase of a wave is simply the angular frequency of the wave, SPM and XPM also appear as a frequency modulation. Thus the pulse experiences a self-induced and cross-induced spectral broadening. It is this effect that accounts for the smooth, featureless spectrum that extends out to the transmission limit of silica fiber (2.25 μm). The continuum on the short-wavelength side of the pump is believed to originate from the FWM process. FWM also accounts for the "filling" of the spectrum between the first few Stokes SRS lines.

A frequency-doubled passively Q-switched microchip laser has been used to generate a supercontinuum in the visible and near-ir portion of the spectrum. The output of this source consists of 5-μJ pulses, ~400 ps in length, at 532 nm. Again, intensities of >10 GW/cm^2 are easily achieved in the fiber core (now single mode in the visible spectral region). A conversion efficiency of 10% is achieved with 0.5-μJ total output. However, in this case, the SRS pulses do not extend into the region of negative group-velocity dispersion. As a result, modulation instability is not present and pulse breakup does not occur. As can be seen in Figure 1-2(b), discreet SRS lines dominate the shorter-wavelength portion of the spectrum. It is only at the longer wavelengths in the near ir that the spectrum becomes truly continuous.

2

327889-3
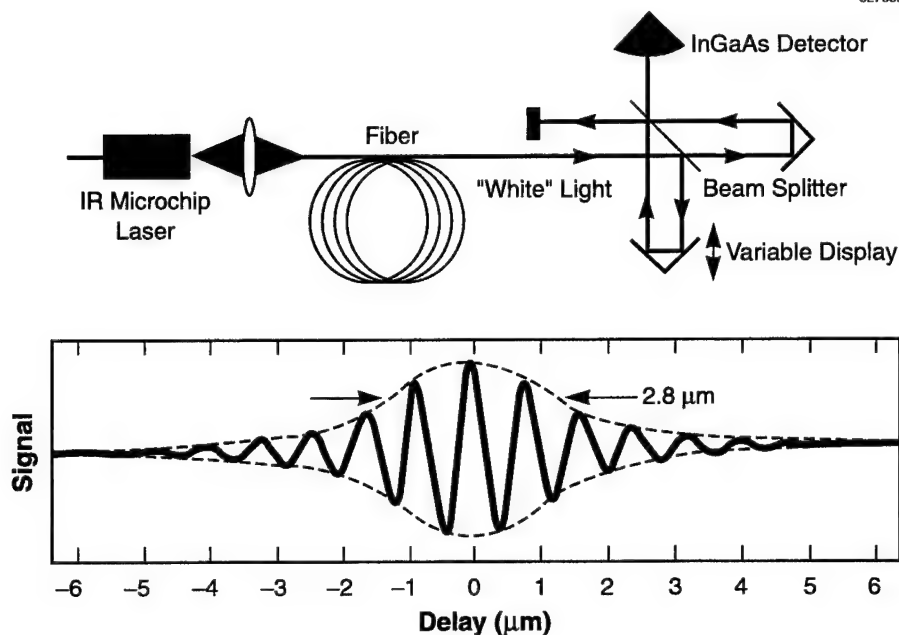
Figure 1-3. White-light interferometry.

One possible application for the source described is in white-light interferometry. Here, the range resolution of the instrument is inversely proportional to the bandwidh of the source. An interferometric autocorrelation trace of the output of the ir-pumped fiber is shown in Figure 1-3. The measured resolution of 2.8 μm is limited by detector response and transmission of the optics. An optimized experiment could improve this figure considerably.

<div align="center">

S. C. Buchter
J. J. Zayhowski

</div>

REFERENCES

1.   J. J. Zayhowski and C. Dill III, *Opt. Lett.* **19**, 1427 (1994).

2.   G. P. Agrawal, *Nonlinear Fiber Optics*, 2nd ed. (Academic, San Diego, 1995).

2. ELECTRO-OPTICAL MATERIALS AND DEVICES

2.1 IMPROVEMENT IN MASS-TRANSPORTED MICROLENSES BY MISORIENTED MESA PREFORMS

Refractive microlenses formed in semiconductors by mass-transport smoothing of etched mesa preforms [1]–[4] hold considerable promise for a wide range of integrated optoelectronics applications. With high refractive indices, microlenses with large numerical apertures can more easily be made with low aberrations. However, deviations from an ideal lens profile must be kept below a few percent of the wavelength in order to ensure diffraction-limited performance with low loss.

Probable causes for profile deviations are any mechanisms that may effect variations in surface energy, the driving force for mass transport, but that are neglected in the simplest mass-transport model used for lens designs. The largest deviations occur when deeply etched tall mesas are used. Indeed, consistent profile deviations similar to these in Figure 2-1(a) have been observed in our recent work, in which mesas of 18-μm height were etched in the fabrication of f/0.5 anamorphic microlenses for tapered lasers of 2-μm wavelength [5]. In that work, a reduction in the deviations was achieved by an empirical correction to the lithographic mask in the mesa definition. However, such compensation procedures must be applied on a case-by-case basis.

In this work, a simple technique that eliminates most of the deviations has been developed based on crystallographic misorientation of the mesa preform. Previously, the axes of the spindle-shaped mesas were aligned parallel to the cleave direction, making the etched mesa sidewalls essentially (011) faces. The lower surface energy of the (011) faces compared to that of the (100) substrate surface [6] represents the dominant mass-transport driving force that is not included in the original design. The effect of crystallographic orientation has indeed been observed and correlated with the more "flat-topped" lens profiles found in our earlier GaP microlenses, as shown in Figure 2-1(a). The effect was more pronounced in our recent development of fast GaAs microlenses.

To avoid the strong (011) faces, the spindle-shaped mesas were misoriented in the present cylindrical microlens fabrication in GaP substrates. In separate wafers, misorientations of 13° and 24° were implemented by rotating the mask in the lithographic definition. The 13° misorientation already resulted in marked deformation reduction, but the 24° one yielded a more complete improvement, as shown in Figure 2-1(b), where relatively small deviations of a few hundred angstroms were measured. Drastic improvements in GaAs microlenses were also observed, and more work is still under way to determine the optimum condition for that material.

The small profile deviation that is still present is expected to result in some relatively small loss. A simple measure of the lens efficiency is the Strehl ratio, which considers the phase deformation across a uniformly illuminated lens and gives the intensity at the center of the far field [7],[8]. For a Gaussian beam, the efficiency is more accurately represented by the weighted Strehl ratio,

$$SR = \left| \int e^{i2\pi(n-1)\delta(x)/\lambda} e^{-x^2/w^2} dx \Big/ \int e^{-x^2/w^2} dx \right|^2 \qquad (2.1)$$

where n is the refractive index of the lens material, $\delta(x)$ is the deviation, λ is the wavelength in air, w characterizes the beam width at the lens, and the integration is over the lens aperture. Since the deviation $\delta(x)$ is measured in the lens profiling as in Figure 2-1, the weighted Strehl ratio in Equation (2.1) can readily be evaluated numerically. With a beam width w of 96 μm, the weighted Strehl ratios calculated for Figures 2-1(a) and 2-1(b) are 0.50 and 0.83, respectively.
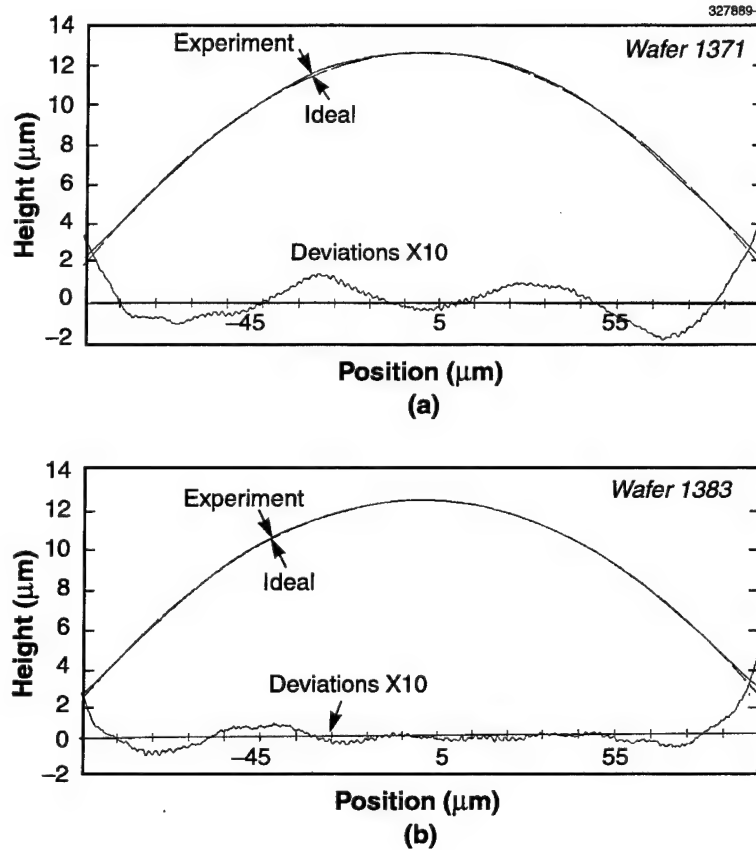
Figure 2-1. Stylus surface profiling of mass-transported GaP cylindrical microlenses which have been fabricated with spindle-shaped mesas (a) parallel to the cleaved (011) face and (b) misoriented 24° with respect to that direction.
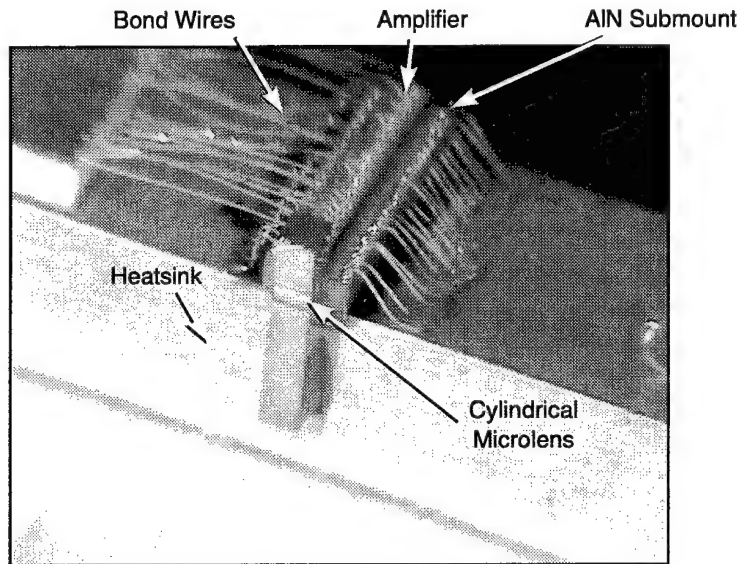
Figure 2-2. Cylindrical microlens chip packaged to tapered amplifier for removal of astigmatism of the output beam.

Figure 2-2 shows a GaP cylindrical microlens, similar to that in Figure 2-1(b), packaged to a 1.3-μm-wavelength InGaAsP amplifier with a 2-mm-long tapered gain region [9]. Here the cylindrical lens has been designed to magnify the source in the direction perpendicular to the junction in order to remove the astigmatism. Also, the effective lens aperture of 190 μm has been designed to make the beam nearly round. Figure 2-3 shows scans of the beam in both directions. Note that the beam has a well-behaved central lobe with little energy in the sidelobes. This partially collimated beam was then focused by a pair of microscope objectives to a single-mode fiber of 8-μm core diameter. The highest coupling efficiency measured was 55% and was already better than the 52% previously achieved by using conventional bulk lenses. When a commercial isolated launcher was used instead of the pair of microscope objectives, the efficiency was 35%. This reduction in efficiency was due to the loss of the isolator and to a mismatch to the optimum beam divergence for the launcher. Further microlens improvement appears possible through more complete deformation reduction, increase in beam collection, and maximization of the beam circularity.

Z. L. Liau   J. N. Walpole

G. E. Betts   L. J. Missaggia

J. P. Donnelly

327889-13P
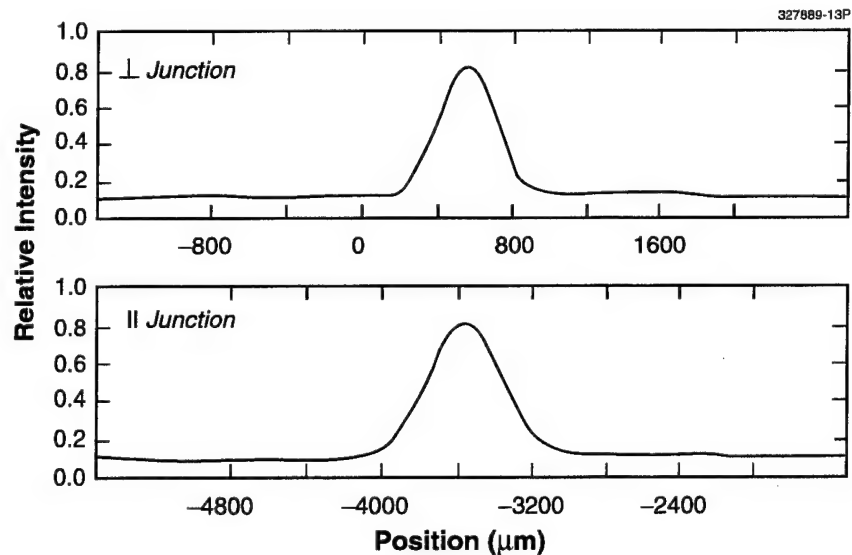
Figure 2-3. Intensity profile of beam of tapered-amplifier/cylindrical-microlens package.

REFERENCES

1. Z. L. Liau, D. E. Mull, C. L. Dennis, R. C. Williamson, and R. G. Waarts, *Appl. Phys. Lett.* **64**, 1484 (1994).

2. Z. L. Liau, J. N. Walpole, D. E. Mull, C. L. Dennis, and L. J. Missaggia, *Appl. Phys. Lett.* **64**, 3368 (1994).

3. J. S. Swenson, Jr., R. A. Fields, and M. H. Abraham, *Appl. Phys. Lett.* **66**, 1304 (1995).

4. F. Nikolajeff, T. A. Ballen, J. R. Leger, and A. Gopinath, to be published in *Appl. Opt.*

5. J. N. Walpole, H. K. Choi, Z. L. Liau, L. J. Missaggia, and G. W. Turner, unpublished material.

6. See, for example, J. M. Blakely, *Introduction to the Properties of Crystal Surfaces* (Pergamon, Oxford, 1973), p. 116.

7. See, for example, M. Born and E. Wolf, *Principles of Optics,* 6th ed. (Pergamon, Oxford, 1980), p. 460.

8. Z. L. Liau, D. Z. Tsang, and J. N. Walpole, *IEEE J. Quantum Electron.* **33**, 457 (1999).

9. J. P. Donnelly, J. N. Walpole, G. E. Betts, S. H. Groves, J. D. Woodhouse, F. J. O'Donnell, L. J. Missaggia, R. J. Bailey, and A. Napoleone, *IEEE Photon. Technol. Lett.* **8**, 1450 (1996).

3. SUBMICROMETER TECHNOLOGY

3.1 LITHOGRAPHIC DOSE CONTROL ERRORS FROM TRANSIENT ABSORPTION IN FUSED SILICA AT 193 nm

A number of recent studies have addressed the degradation of fused silica under excimer laser irradiation with applications in microlithography [1]–[6]. In their assessment of optical properties relevant for lithographic applications, these studies concentrated on permanent changes that resulted from irradiation, such as induced absorption of fused silica and compaction. Additionally, a number of authors have also reported a phenomenon in fused silica termed transient absorption [1],[7],[8]. This phenomenon, believed to be a bulk effect, refers to a temporary reduction in transmission as the fused silica is exposed to the laser, and a subsequent recovery when the laser is turned off. According to a recent model [1], transient absorption can be understood in terms of recombination processes of dissolved hydrogen with fused silica E′ centers.

Under a cooperative research and development agreement with SEMATECH, we have assessed transient absorption in conjunction with a comprehensive study of optical material lifetimes [3]. In that study a large number of production- and research-grade samples were irradiated for several billion pulses each at incident fluences ranging from 0.25 to 4 mJ/cm^2/pulse. For this report, we present results on rectangular samples with nominal dimensions of $80 \times 40 \times 20$ mm that were irradiated along their longest axis.

The transient absorption studies were performed in a separate nitrogen-purged laser ratiometric system. In this setup, light from a 193-nm laser source operating at 200 Hz was incident on a 50/50 beamsplitter, positioned at 45°. The reflected light (reference beam) and transmitted light (sample beam) impinged on two separate detectors. Both pyroelectric and silicon-diode-based detectors were used, depending on the incident fluence. The sample under measurement was placed on a computer-controlled shuttle that translated in and out of the sample beam. The ratio of the readings of the two detectors was recorded on a pulse-by-pulse basis, and the transmission was obtained by averaging 200 ratios at a time. Every time a transmission reading was obtained, the baseline ratio of the two detectors was also measured with the sample out of the beam to account for drifts in detector response. During the illuminated-state measurements the sample remained in the laser beam except for a brief interval (≈ 2 s) every time a data point was acquired to collect a reference reading. For the dark-state measurements, the reverse procedure was applied: the sample remained outside the laser beam except for a brief interval when the transmission measurement is obtained. The duty cycle of both measurement states was about 96%.

The data presented here are shown as total absorption per unit length, base 10, obtained from these in-situ transmission data, and accounting for Fresnel reflection losses, surface scatter/absorption losses, and bulk scatter as described earlier [9]. Our absorption measurement repeatability for the lowest incident fluence (≈ 0.05 mJ/cm^2/pulse) was $\approx 2 \times 10^{-5}$/cm, one standard deviation, which would correspond to an ability to detect 0.2% transmission changes for a 50-cm path of fused silica with a nominal absorption coefficient of 0.002 cm^{-1}. The temporal resolution of transient effects in our experiment was ≈ 1 s.

Typical time-resolved absorption data are shown in Figure 3-1. We note that the magnitude of the transient absorption, excepting an initial larger rise, is ≈0.00013/cm, or about 6% of the total absorption, with the time scale for the onset and decay of several minutes. We also note that the initial change in absorption is about 2.5× larger than the subsequent magnitude of the transient. This observation suggests that some component of absorption may relax on the time scale of hours in addition to faster processes depicted in Figure 3-1.

In Figure 3-2 we show results of transient absorption measurements performed at different fluences. As the fluence of the transient measurement was reduced by a factor of ≈40, from 1.5 to 0.04 mJ/cm^2/pulse, the magnitude of the effect was reduced by only a factor of 2.5. The 1/e onset time increased by more than a factor of 4 when the fluence dropped from 0.25 to 0.04 mJ/cm^2/pulse. It is evident from Figure 3-2 that extrapolation from higher fluence data down to lithographic fluences would not be reliable without predetermination of such scaling trends.

In order to assess the impact of transient absorption on a lithographic system, we estimate its effect on dose variation. We assume that the steady-state absorption value is 0.002/cm, the transient swing is 0.0002/cm, and the 1/e time constant for the absorption onset is 5 min. Based on our transient measurements, such values would be typical for incident fluences of ≤0.1 mJ/cm^2/pulse. We further assume a total fused silica length of 50 cm in a projection lens system and a throughput of 60 wafers per hour. Figure 3-3 shows the expected dose error in percent as a function of the number of wafers. The final dose error due to transient absorption approaches 2%, the total allowable dose error budget from all the effects in the exposure tool. The implicit assumption in Figure 3-3 is that the laser light had been shuttered for >>5 min prior to exposing the first wafer, and that the time constant of the transient is long compared to the time between exposure of individual die and wafers (seconds). From Figure 3-3 it is clear that some form of transient
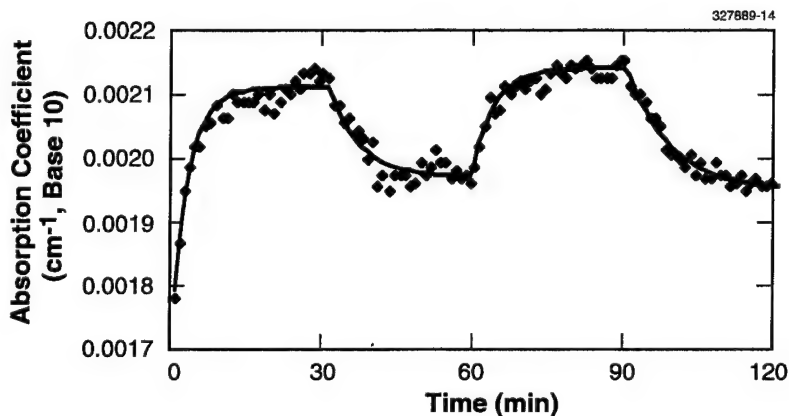
Figure 3-1. Time-resolved absorption data for 8-cm-long fused silica sample that had been preirradiated at 0.6 mJ/cm^2/pulse for 4 × 10^9 pulses. Experimental data (points) were obtained at an incident fluence of 0.25 mJ/cm^2/pulse. The solid line is a fit to a single exponential. The sample is in the illuminated state from 0 to 30 min and 60 to 90 min. The sample is in the dark state from 30 to 60 min and 90 to 120 min.
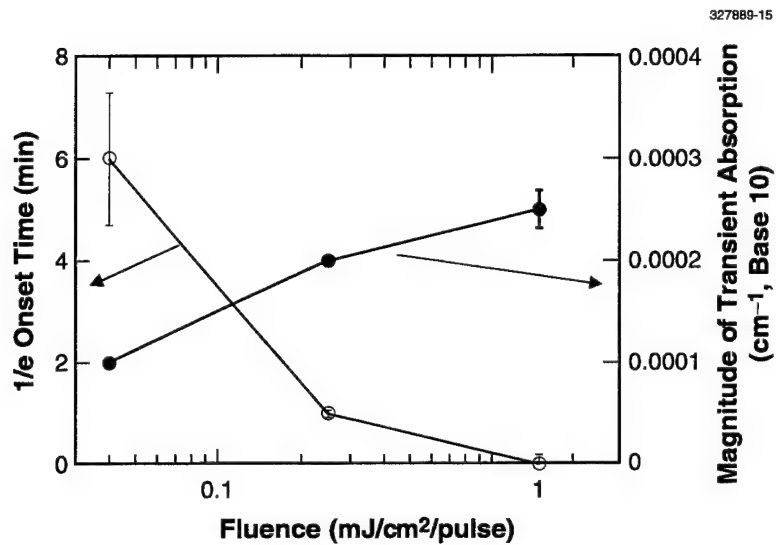
Figure 3-2. *Fluence-dependent behavior of onset time and the magnitude of transient absorption. The sample had been preirradiated for* 2×10^9 *pulses at 1 mJ/cm^2/pulse.*
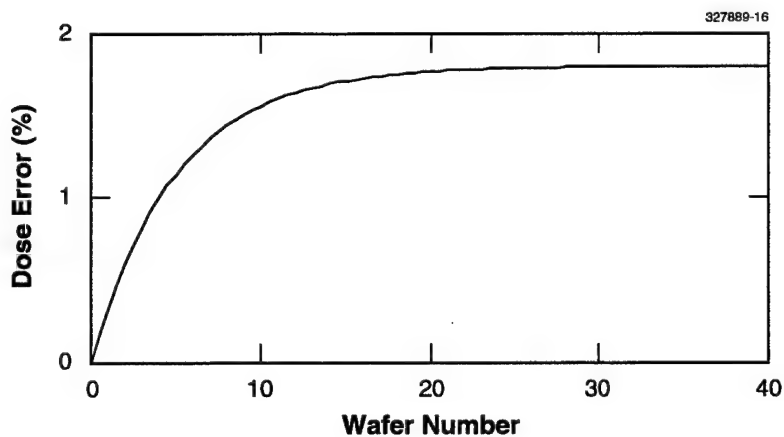
Figure 3-3. *Dose error resulting from effects of transient absorption as a function of time (in wafers processed, assuming 1 wafer per minute). See text for underlying assumptions.*

absorption compensation will be required in a projection system to keep the transient contribution from dominating the dose control budget. Simple compensation algorithms may involve precharacterization of the transient behavior of lens materials or preirradiation of the lens for several minutes prior to onset of exposures. Alternatively, a larger fraction of optical elements may need to be manufactured out of calcium fluoride to minimize effects of transient absorption.

V. Liberman   A. Grenville
M. Rothschild   A. K. Bates
J. H. C. Sedlacek

3.2 LARGE-AREA INTERDIGITATED ARRAY MICROELECTRODES FOR ELECTROCHEMICAL SENSING

Electrochemical detection has been used in various forms for well over 50 years. Recently, the miniaturization of analytical instrumentation has led to the exploration of planar miniaturized electrochemical devices. In fact, very closely spaced electrodes offer performance advantages over macroscopic devices, and various microelectrode geometries have been investigated in attempts to increase their detection sensitivity by minimizing the effects of analyte depletion and the double-layer charging current during measurement of reversible redox species. One geometry that has drawn particular interest is that of interdigitated arrays (IDAs) of microelectrodes. In the IDA configuration one electrode is held at a potential to drive the reduction $O + ne \rightarrow R$, while the other electrode is held at a potential to drive the oxidation $R \rightarrow O + ne$. Species produced at one electrode diffuse to the other electrode, where they are converted back to their original form, creating a process called redox cycling. This cycling between the two electrodes can lead to a greatly amplified current because the analyte is never depleted. This was first demonstrated by Bard and coworkers [10] in 1986 using two photolithographically patterned microelectrodes, the generator and collector electrodes. Decreasing the dimensions of the electrodes and the interelectrode gap increases the cycling efficiency, because fewer reacted redox species diffuse back into the bulk solution. Quantitative analyses of such IDAs have been developed [10]–[12], and electrodes spaced as closely as 800 nm have been fabricated [12]. For most of these scaled devices, redox cycling efficiencies (i.e., faradaic current enhancements) on the order of 40 have been reported. The only example of redox cycling using deep submicrometer interelectrode gaps was achieved with a modified atomic force microscope tip [13], where faradaic currents corresponding to redox species' cycling frequencies in excess of ~10^6 Hz were reported for an interelectrode gap of 15 nm. We report the fabrication of scaled IDAs using state-of-the-art yet practical lithographies. We also report on the performance of these sensors, which have a sensitivity higher than any other IDAs, and analyze the advantages enabled by lithographic scaling. In fact, a straightforward extension of the fabrication method used in our experiments has the potential to generate practical IDAs with a sensitivity of <1 ppb of analyte at response times in the millisecond range. This would represent a performance regime not yet realized in IDA sensors.

Five sensors have been fabricated, each consisting of an interdigitated electrode array, shown in Figure 3-4. The finger length b is 2 mm in all arrays. The electrode width w_f is varied from 0.5 to 5 μm, and the electrode gap w_g is varied from 0.15 to 5 μm. Each array has an active area of $(2 \text{ mm})^2$. The patterning process is illustrated in Figure 3-5. A deep-ultraviolet exposure tool operating at 193 nm replicated the sensor pattern. The resist used was a poly(vinyl phenol) resin, which acts as a top-surface imaged dry-developed resist [14]. This type of resist allows control over the developed profiles to obtain slight overhangs, thereby facilitating the subsequent metal liftoff step. Following photoresist patterning, a platinum liftoff was performed. Figure 3-6(a) shows an electron micrograph of a reentrant resist profile created using this process and Figure 3-6(b) shows a completed sensor.

327889-17
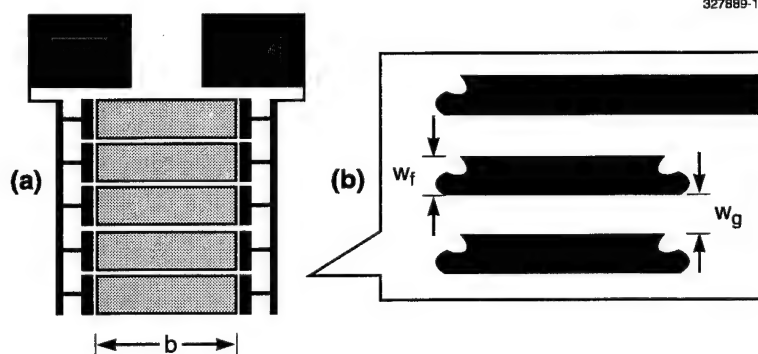
Figure 3-4. Layout of the interdigitated sensor showing (a) macroscopic configuration with the contact pads on top and (b) microscopic configuration. The b is finger length, w_f is electrode width, w_g is interelectrode gap, and m (not shown) is the number of pairs of fingers.

The redox cycling ability of the arrays was tested in an aqueous solution of $Ru(NH_3)_6^{3+}$ in 0.1-M $KCl_{(aq)}$, and in dinitrotoluene in 0.2-M tetrabutylammonium perchlorate in acetonitrile. All reagents were used as received. Cyclic voltammograms were recorded on a potentiostat/galvanostat with a home-built second potentiostat channel [15]. In aqueous solution, voltages were measured and are reported with respect to an Ag/AgCl reference electrode, and in acetonitrile, voltages were measured and are reported with respect to an Ag/AgNO₃ organic electrochemistry reference electrode. Data from the potentiostat were digitized and recorded on a personal computer.

We first measured the redox current for an aqueous solution of $Ru(NH_3)_6^{3+}$ in a conventional three-electrode arrangement (Figure 3-7(a), generator, no feedback) and compared it to the current with a potential applied to the fourth, collector electrode (Figure 3-7(a), generator, with feedback). Our results demonstrate that the faradaic signal is significantly enhanced when the array performs redox cycling. Table 3-1 shows the performance characteristics of all five arrays in the $Ru(NH_3)_6^{3+}$ solution. The **C** electrodes give a signal of 232 nA/μM analyte, while the **A** electrodes pass 176 nA/μM analyte (Table 3-1). Figure 3-8
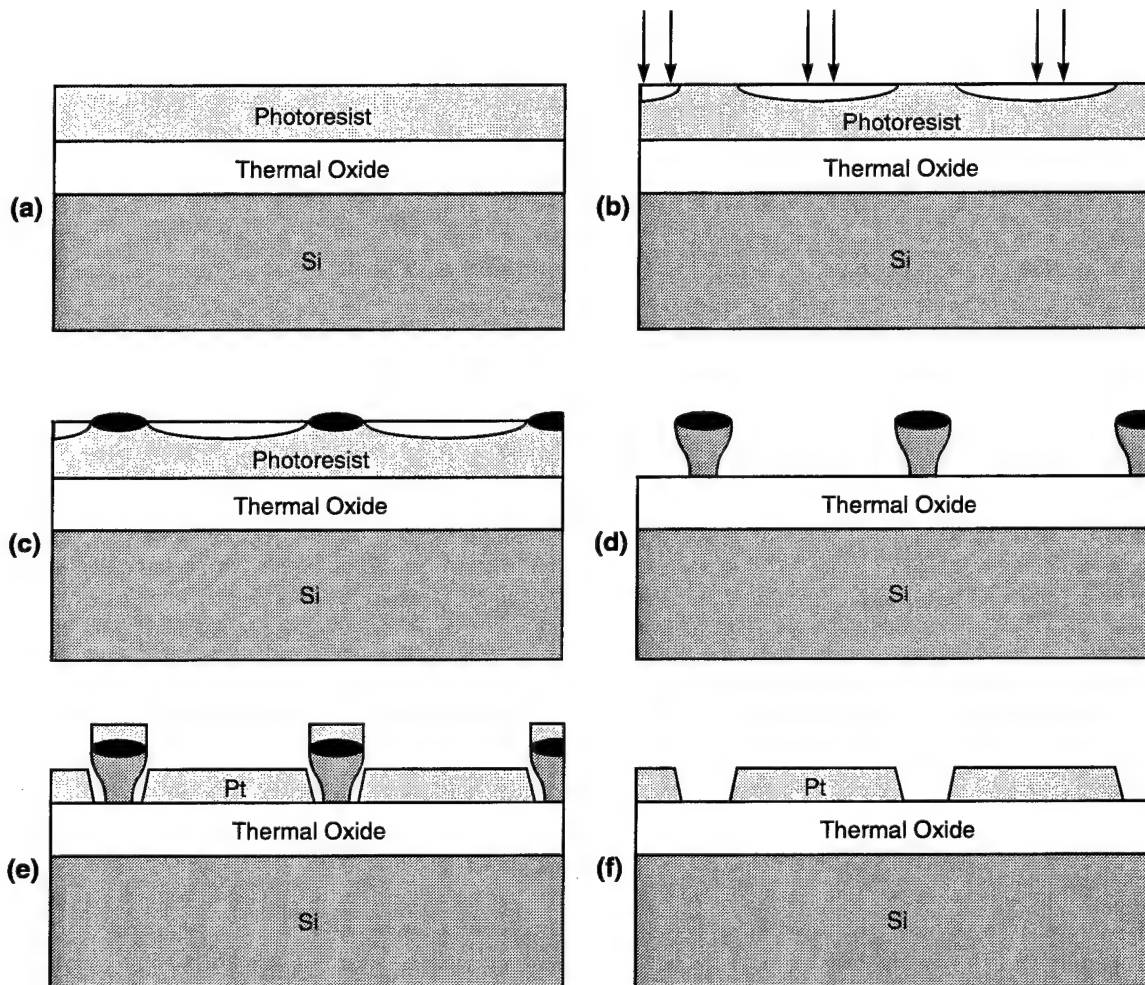
Figure 3-5. (a) Thermal growth of 500-nm oxide on a silicon wafer, followed by coating of the oxide with poly(vinyl phenol), which acts as dry-developed resist; (b) exposure in 193-nm, 0.5-numerical-aperture (NA) projection system; (c) silylation using dimethylsilyldimethylamine; (d) dry development to generate reentrant profile; (e) evaporation of 100-nm Pt onto wafer; and (f) removal of remaining photoresist by ultrasonic agitation for 1 h in EKC 265 resist stripper at 55°C, leaving the desired pattern on the wafer.
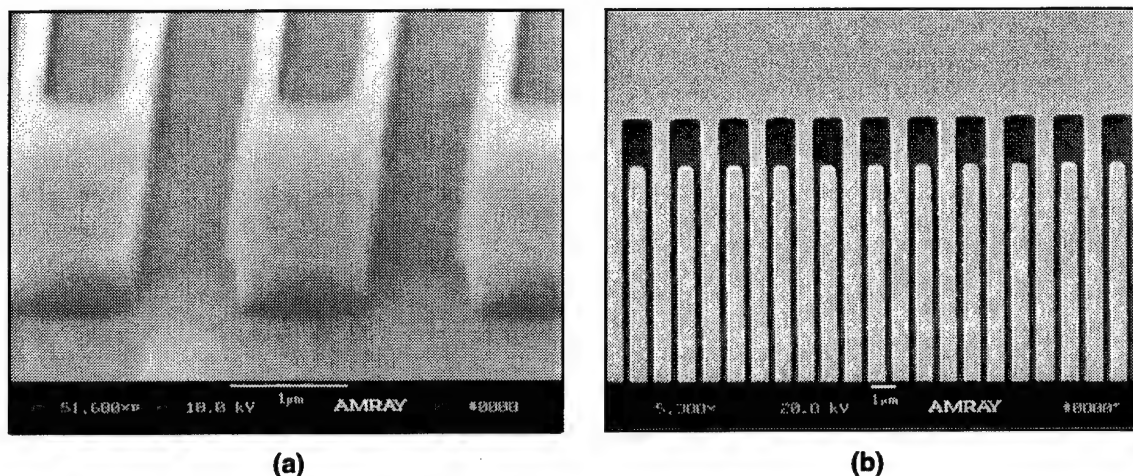
*Figure 3-6. Electron micrographs of (a) reentrant resist profile and (b) completed sensor (array **B** in Table 3-1).*

TABLE 3-1
Performance of Five Arrays in 1-mM $Ru(NH_3)_6^{3+}$ in 0.1-M KCl*

Array	w_g (μm)	w_f (μm)	b (mm)	m	I_{lim}[†] (μA)	I_{lim}[‡] (μA)	Gain	Φ (m)
L	5	5	2	100	4.8	17.5	3.6	0.20
A	0.5	0.5	2	1000	4.5	176	39	2.0
B	0.25	0.75	2	1000	4.5	218	48	2.9
C	0.2	0.80	2	1000	4.8	232	48	3.2
D	0.15	0.85	2	1000	6.4	220	34	3.6

*The array characteristics are w_g (interelectrode gap), w_f (finger width), b (finger length), and m (number of pairs of fingers). To measure I_{lim} without feedback, the potential was swept at 5 mV/s. The gain is calculated by dividing the limiting current with feedback by the limiting current without feedback. Φ is a geometric factor described by Aoki et al. [16].

[†]No feedback, collector open circuit.

[‡]Collector at +0.1 V.
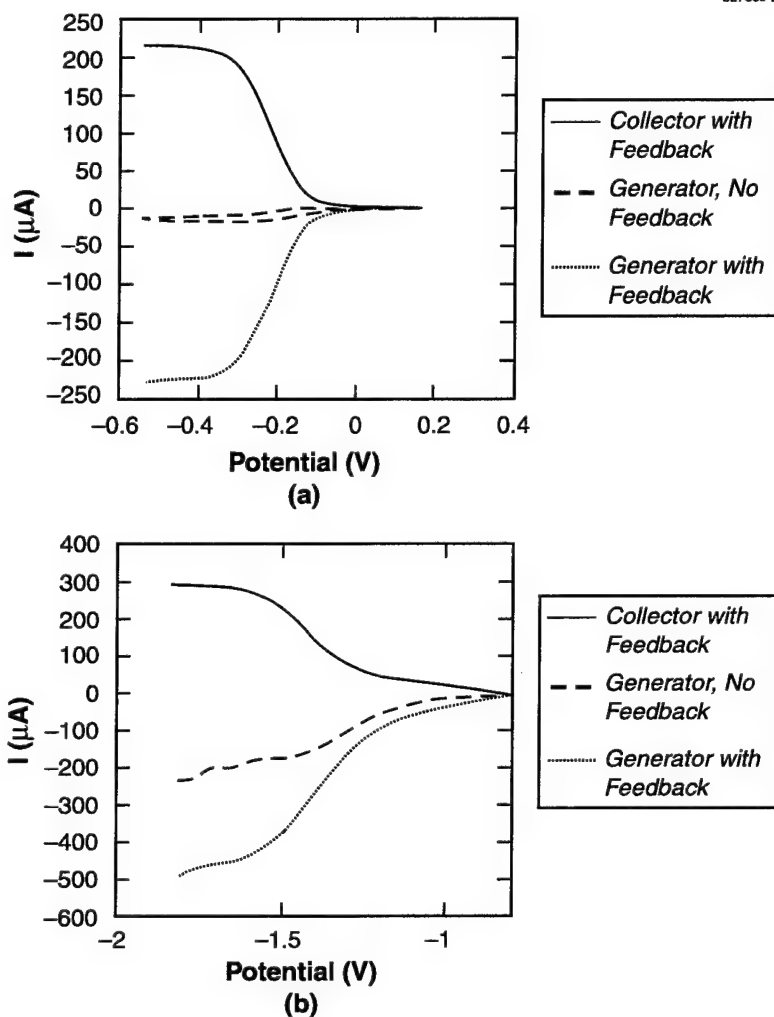
*Figure 3-7. (a) Redox cycling in array **D** (see Table 3-1) in 1-mM Ru(NH₃)₆³⁺ in 0.1-M KCl; sweep rate = 50 mV/s; with feedback, collector potential = 0.1 V vs Ag/AgCl. (b) Redox cycling in array **B** (see Table 3-1) in 1-mM dinitrotoluene in 0.2-M tetrabutylammonium perchlorate in acetonitrile; sweep rate = 50 mV/s; with feedback, collector potential = –0.8 V vs Ag/AgNO₃.*

16
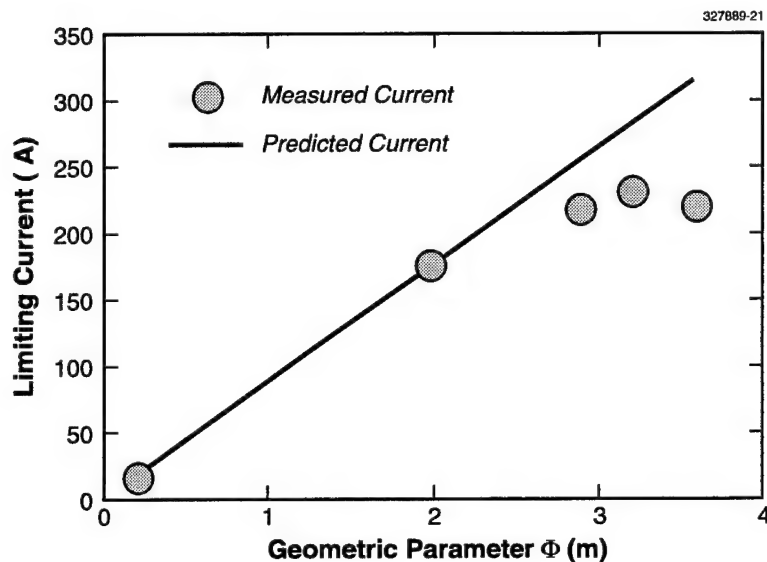
Figure 3-8. Limiting current as a function of geometric parameter Φ, defined by Aoki et al. [16]. The drop in current below the predicted value [16] for large values of Φ is probably the result of defects in arrays with very small geometries, although other possible explanations have not been ruled out.

shows the redox cycling current for $Ru(NH_3)_6^{3+}$ solutions for all four arrays tested versus a geometric parameter Φ (to be discussed a bit later). This parameter, which has units of distance, describes the proximity of the generator and collector electrodes. The current in the **A** array reaches its steady-state value within 5 ms after the feedback is turned on. An **A** electrode operated continuously in solution with little change in current for almost one and a half hours. In addition we used nonaqueous solutions of dinitrotoluene and observed signals of 500 nA/μM, as seen in Figure 3-7(b). However, this represents only a 2× gain over the three-electrode configuration compared to the 40–50× enhancements we saw in the aqueous $Ru(NH_3)_6^{3+}$ solutions.

The limiting current for the **B**, **C**, and **D** electrodes in $Ru(NH_3)_6^{3+}$ solution is lower than that predicted by the current accepted theory [16] by 15, 19, and 31%, respectively. We tentatively attribute this deviation to possible defects on the arrays tested, which prevent redox cycling from occurring in some sections of the arrays. Our electrical inspection of the arrays revealed consistently high values of interelectrode resistance (>0.1 MΩ) for the **L** and **A** arrays (it was not infinite because of residual surface conductivity of the SiO_2 substrate). However, we found interelectrode resistance values to vary from array to array for the **B**, **C**, and **D** arrays. Although our lithographic techniques are easily capable of yielding defect-free devices of this size and geometry, we know that the platinum liftoff step is prone to producing metallic particles which can cause electrical shorts. Owing to the relatively high resistance of the electrode fingers themselves (~1 kΩ), however, a single short circuit might not render an entire array inoperable.

17

Some fingers in the arrays may also have been disconnected from the voltage supply. However, other reasons for the deviation of experimental results from the predicted linear behavior, shown in Figure 3-8, have not been ruled out.

Our experiments partially close the gap between the dimensions attained in proximal probe electrochemistry experiments [13],[17] and those achieved by conventional photolithography. The benefit of smaller electrode geometries can now be practically realized simply from the fact that with smaller electrodes, more of them can be photolithographically patterned into a fixed area. In fact, using the same exposure tool used to fabricate these $(2 \text{ mm})^2$ arrays, devices whose overall area was $(20 \text{ mm})^2$ would have been just as easy to fabricate, further increasing the signal by another factor of 100 (with probably a somewhat lesser increase in noise as well). Even though the resultant arrays would now have occupied 400 mm^2, such a mass-produced device whose sensitivity was on the order of ~25 nA/nM (i.e., 25 nA at a concentration of ~20 parts per trillion) and with a response time of tens of milliseconds, could offer utility for certain monitoring applications such as liquid chromatography [18]–[20], meso- and micro-scale fluidics, and process monitoring. In addition, our detection of dinitrotoluene suggests that IDAs can be used to detect other nitroaromatic compounds used in explosives, possibly in applications such as groundwater contamination.

A. E. Cohen*
R. R. Kunz

---

*Author not at Lincoln Laboratory.

REFERENCES

1. R. J. Araujo, N. F. Borrelli, and C. Smith, *Proc. SPIE* **3424**, 2 (1998).

2. C. Smith, N. F. Borrelli, D. C. Allan, and T. P. Seward, *Proc. SPIE* **3051**, 116 (1998).

3. V. Liberman, M. Rothschild, J. H. C. Sedlacek, R. S. Uttaro, A. Grenville, A. K. Bates, and C. Van Peski, *Opt. Lett.* **24**, 58 (1999).

4. V. Liberman, M. Rothschild, J. H. C. Sedlacek, R. S. Uttaro, A. Grenville, A. K. Bates, and C. Van Peski, *Proc. SPIE* **3427**, 411 (1998).

5. T. Westerhoff, K. Knapp, and E. Moersen, *Proc. SPIE* **3424**, 10 (1998).

6. S. Thomas and B. Kuhn, *Proc. SPIE* **2966**, 56 (1996).

7. V. Uhl, K. O. Greulich, and S. Thomas, *Appl. Phys. A* **65**, 457 (1997).

8. N. Leclerc, C. Pfleiderer, H. Hitzler, J. Wolfrum, K. O. Greulich, S. Thomas, and W. Englisch, *J. Non-Cryst. Solids* **149**, 115 (1992).

9. D. Cote, K. Andresen, D. Cronin, H. Harrold, M. Himel, J. Kane, J. Lyons, L. Markoya, C. Mason, D. McCafferty, M. McCarthy, G. O'Connor, H. Sewell, and D. Williamson, *Proc. SPIE* **3051**, 806 (1997).

10. A. J. Bard, J. A. Crayston, G. P. Kittlesen, T. Varco Shea, and M. S. Wrighton, *Anal. Chem.* **58**, 2321 (1986).

11. B. Fosset, C. A. Amatore, J. E. Bartelt, and R. M. Wightman, *Anal. Chem.* **63**, 1403 (1991).

12. B. Fosset, C. A. Amatore, J. E. Bartelt, A. C. Michael, and R. M. Wightman, *Anal. Chem.* **63**, 306 (1991).

13. F. F. Fan, J. Kwak, and A. J. Bard, *J. Am. Chem. Soc.* **118**, 9669 (1996).

14. S. C. Palmateer, R. R. Kunz, M. W. Horn, A. R. Forte, and M. Rothschild, *Proc. SPIE* **2438**, 455 (1995).

15. A. J. Bard and L. Faulkner, *Electrochemical Methods: Fundamentals and Applications* (Wiley, New York, 1980), pp. 566-567.

16. K. Aoki, M. Morita, O. Niwa, and H. Tabei, *J. Electroanal. Chem.* **256**, 269 (1988).

17. F. F. Fan and A. J. Bard, *Science* **267**, 871 (1995).

18. O. Niwa, M. Morita, and H. Tabei, *Sensors and Actuators B* **13-14**, 558 (1993).

19. O. Niwa, M. Morita, and H. Tabei, *Electroanalysis* **6**, 237 (1994).

20. M. Takahashi, M. Morita, O. Niwa, and H. Tabei, *J. Electroanal. Chem.* **335**, 253 (1992).

4. BIOSENSOR AND MOLECULAR TECHNOLOGIES

4.1 DEVELOPMENT OF GENETICALLY ENGINEERED FIBROBLAST CELLS FOR A BIOELECTRONIC SENSOR

Previously, we described a sensor for the detection of viral and bacterial pathogens which exploits the natural immune response [1]. The cornerstone of the CANARY (Cellular Analysis and Notification of Antigen Risks and Yields) sensor is a cell line derived from a white blood cell, called a B cell, which expresses antibodies on the outer membrane specific for a particular molecule (antigen). Antibody-antigen interaction generates a signal inside the B cell which undergoes several levels of amplification and causes increase in the internal calcium-ion concentration. We engineered an immortal B-cell line to permanently express the jellyfish aequorin gene, a protein that generates light in the presence of both high levels of calcium and the substrate coelenterazine, thereby achieving cells that emit photons upon antigen binding.

In addition to the modifications necessary for the cells to express exogenous (genetically engineered) antibodies on the surface, we are concentrating on several features required of the cells in order to assemble them within the hardware of the sensor. The cells must attach to the substrate, and they must not overgrow the designated address, nor detach and colonize an area specific for a different antigen. Since the immortal B cell lines will normally divide every 18–24 hours and would rapidly overpopulate a given area, we have investigated both chemical and physical methods of inhibiting their growth. As shown in Figure 4-1, we are able to control B cell growth by reducing the culture temperature from 37 to 28°C. This has been demonstrated by two assays. The first, in Figure 4-1(a), shows that the level of DNA synthesis has been reduced from 34% to 5%, and the second, in Figure 4-1(b), shows that labeled cells decrease steadily in fluorescence intensity as they divide at 37°C, but remain stable at the lower temperature.

While B cells are naturally designed to detect foreign invaders, they must be modified to be integrated into the hardware of the sensor. As an alternative approach, we are simultaneously developing another cell type that is ideal for integration into the sensor, but must be modified to detect antigen. Fibroblasts are cells which are very adherent and exhibit a quality known as contact inhibition, where cell-to-cell contact causes cessation of growth without cell death. We have been able to maintain fibroblasts under conditions of contact inhibition for as long as 60 days without observing free cells in the medium. This indicates that a sensor populated with fibroblasts will have a life span of at least 2 months and will be free of cross-contamination or overgrowth problems.

Unlike the B cells, fibroblasts are not natural detectors of foreign molecules. However, they do share some of the circuitry that might be harnessed to produce an aequorin signal in response to antigen [2]. Fibroblasts have, on their surface, a protein called the fibroblast growth factor receptor (FGFR). The binding of a soluble protein, fibroblast growth factor, brings together two receptors, like the dimerization of antibodies on the surface of a B cell. Receptor dimerization initiates a signal transduction cascade that produces an increase in calcium concentration which will support the function of aequorin, as shown in Figure 4-2(a). In order to provide a specific response to antigen, we are engineering a chimeric antibody-FGFR

DNA Synthesis (4 hr)

37°C ███████████████████ 34%

28°C ▢ 5%

Percent of Cells

(a)

37°C

28°C

Day 1
Day 2
Day 3
Day 4

(b)
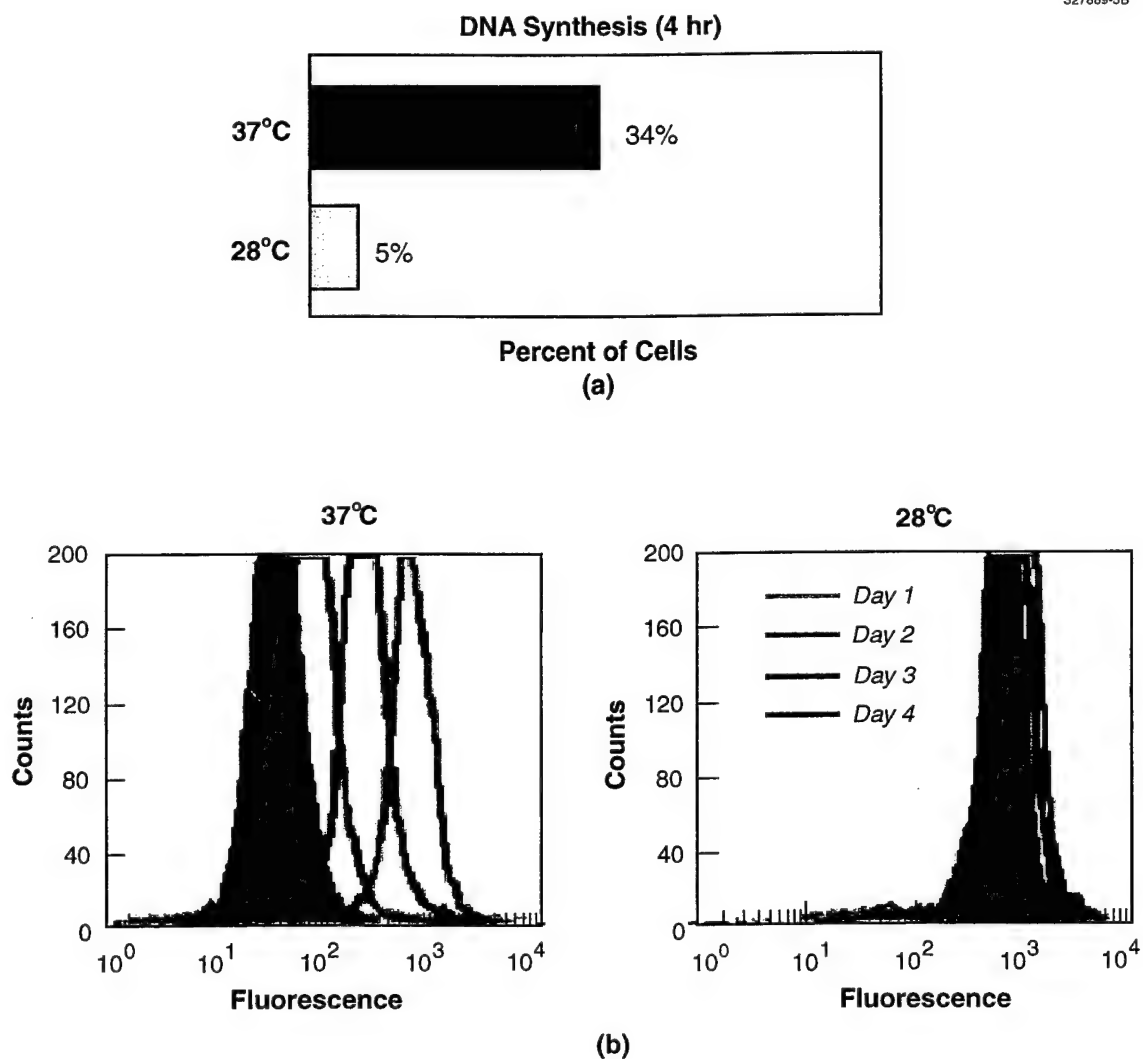
Figure 4-1. Growth control of B cells: (a) DNA synthesis is inhibited in B cells cultured at lower temperature, and (b) cell division does not occur when B cells are cultured at a lower temperature.

22

Calcium Response

327889-6B

(a)

(b)

Fibroblasts   B Cells
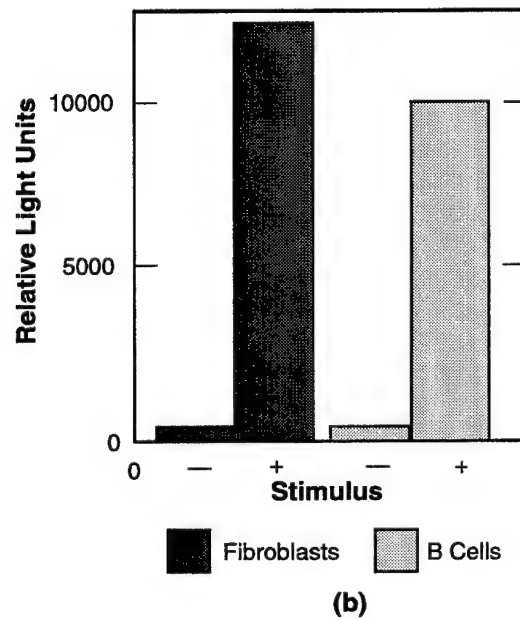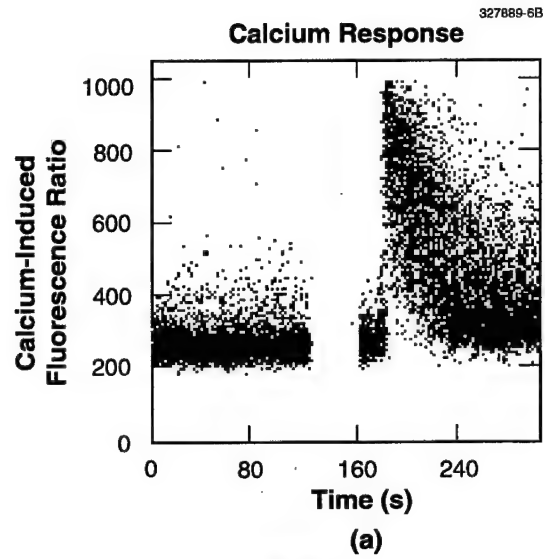
Figure 4-2. Fibroblast as alternative to B cells: (a) Fibroblasts demonstrate increase in calcium ions in response to stimulus and (b) have potential of emitting as much light as observed with B cells.

molecule, with the intracellular signaling portion of the FGFR and the extracellular portion consisting of the antigen-binding region of the antibody, to be displayed on the surface of fibroblasts. We intend to show that fibroblasts engineered to contain aequorin and this so-called chimeric receptor will glow upon antibody-antigen interaction.

Towards this goal, we have constructed a DNA vector which contains the genetic material encoding the desired portions of the FGFR and all of the material which allows high-level expression on the surface of the cell. In addition, we have obtained several pieces of DNA that encode antibodies specific for different bioagent simulants, which we are preparing to insert into the vector. Finally, we are in the process of generating fibroblast lines that are engineered to express aequorin, and in the initial experiments have demonstrated that the fibroblasts have the potential of emitting as much light as observed with the B cells, as seen in Figure 4-2(b). In the near future, we will be concentrating on proving the feasibility of this approach by demonstrating that the specificity of the antibody is maintained, and that the chimeric receptor generates similar levels of calcium concentration as the unaltered FGFR.

T. H. Rider   M. S. Petrovick
A. M. Young   L. T. Smith
M. A. Hollis   J. Chen

REFERENCES

1. Solid State Research Report, Lincoln Laboratory, MIT, 1998:4, p. 27.

2. L. Munaron, C. Distase, V. Carabelli, F. M. Baccino, G. Bonelli, and D. Lovisolo, *J. Physiol.* **484**, 557 (1995).

5. MICROELECTRONICS

5.1 IMPROVED BLOOMING CONTROL FOR BACK-ILLUMINATED CCD IMAGERS

When a charge-coupled device (CCD) imager views a scene with very bright features, the photogenerated electrons may locally overload the pixels. Unless provisions are made for disposing of this excess charge at the pixel level the electrons will spread laterally into adjacent unfilled pixels resulting in a phenomenon called blooming. Apart from being cosmetically objectionable in consumer applications, the bloomed signal charge will obscure portions of the remaining scene and therefore be a problem in applications such as surveillance or astronomy. Blooming control is therefore an important feature of sensors in a variety of applications that must deal with a large intrascene dynamic range. In space surveillance or astronomy, for example, a sensor that integrates long enough to just detect an object of 20th visual magnitude will saturate on stars brighter than about 10th magnitude. Given the large number of stars brighter than 10th magnitude, a CCD on a wide field-of-view telescope will likely encounter blooming in any given field.

Conventional CCD images typically use a blooming control consisting of a reverse-biased pn junction beneath the pixel to collect excess charge. Such an approach cripples the quantum efficiency beyond 600 nm by restricting the photosensitive depth of the pixel to a few micrometers, and in addition it is physically incompatible with back illumination. For back-illuminated imagers a lateral blooming-control structure, illustrated in cross section in Figure 5-1 for the case of an n-channel device, has been used [1]. Here the conventional p^+ channel stop is replaced with an n^+ blooming drain straddled on both sides by lightly doped n^- regions. The threshold voltage of the n^- regions determines the barrier height between the CCD well and blooming drain, and if set properly will allow excess pixel charge to flow into the blooming drain before such charge can spread into adjacent pixels. A buried p^+ layer below the blooming drain and blooming barrier regions is necessary to deflect photoelectrons to the buried channel so that they are not collected by the drain.

We have developed a fabrication technique for a lateral blooming control which requires a single mask step and results in a relatively compact structure. The process steps are illustrated in Figure 5-2. Before the blooming-control steps, the gate dielectric (SiO_2 and Si_3N_4) has been formed on the wafer surface followed by a blanket buried-channel implant of phosphorus. The mask level defining the blooming control is then patterned in photoresist with an opening of nominally 2 μm. A near-vertical arsenic implant (5×10^{14} cm^{-2} at 200 keV) forms the shallow n^+ blooming drain. We then implant boron at a dose and energy of 5×10^{12} at 375 keV at an angle of 45° to the wafer surface with the wafer rotating during the implant. Rotation is used in order to ensure that blooming drains lying along different directions will all have the same barrier threshold. In the region directly beneath the As implant the boron forms a photoelectron barrier with a peak doping of about 5×10^{17}. However, in the regions to the side of the n^+ drain the buried-channel implant is partially compensated by the boron that passes through the sidewalls of the photoresist. This region forms the n^- blooming barrier and is about 0.7 μm wide. This width is set by the boron implant angle and energy, rather than the photolithography, and could be much narrower. Likewise, the

Blooming Drain   Gate

(a)

Potential under
Adjacent Gates

ϕ_1

ϕ_2

ϕ

(b)
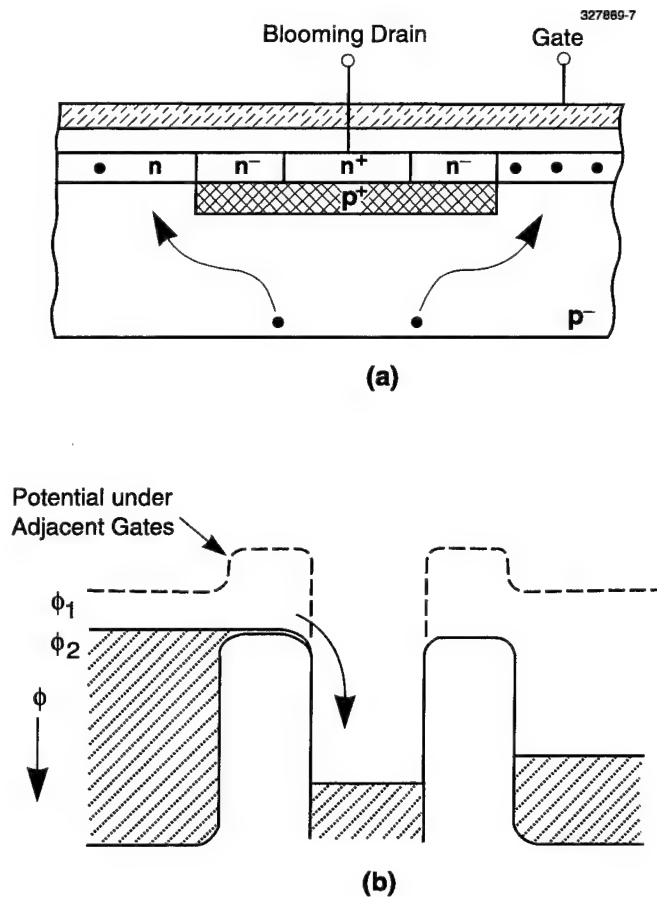
Figure 5-1. Depiction of (a) lateral blooming control suitable for back-illuminated imagers and (b) electrical potential ϕ in the structure.

blooming drain could readily be made narrower than 2 μm, so that a more compact structure appropriate for pixel sizes below 10 μm should be achievable. Figure 5-3 illustrates a simulation of the dopant distribution after the implants but with the photoresist still in place. The shallow high-concentration arsenic implant is the bright red band near the surfaces of the photoresist and the silicon. The phosphorus buried channel, performed prior to the photoresist deposition, is originally a uniform band about 0.4 μm deep across the width of the structure.

The blooming control requires specific clock levels in order to function properly. To determine these levels we measure the potentials in the CCD channel and blooming barrier using test structures on the die next to the imager. These potentials as a function of gate voltage are shown in Figure 5-4. From Figure 5-1 it is clear that the CCD well potential ϕ_1 under the adjacent gates held at a low potential must be less than

26
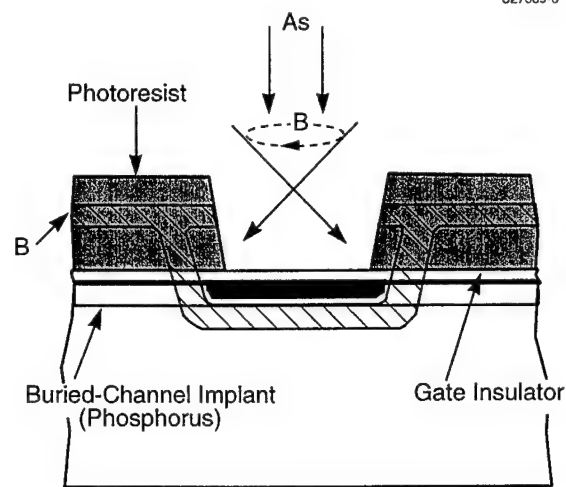
Figure 5-2. Illustration showing implants used to create blooming control.
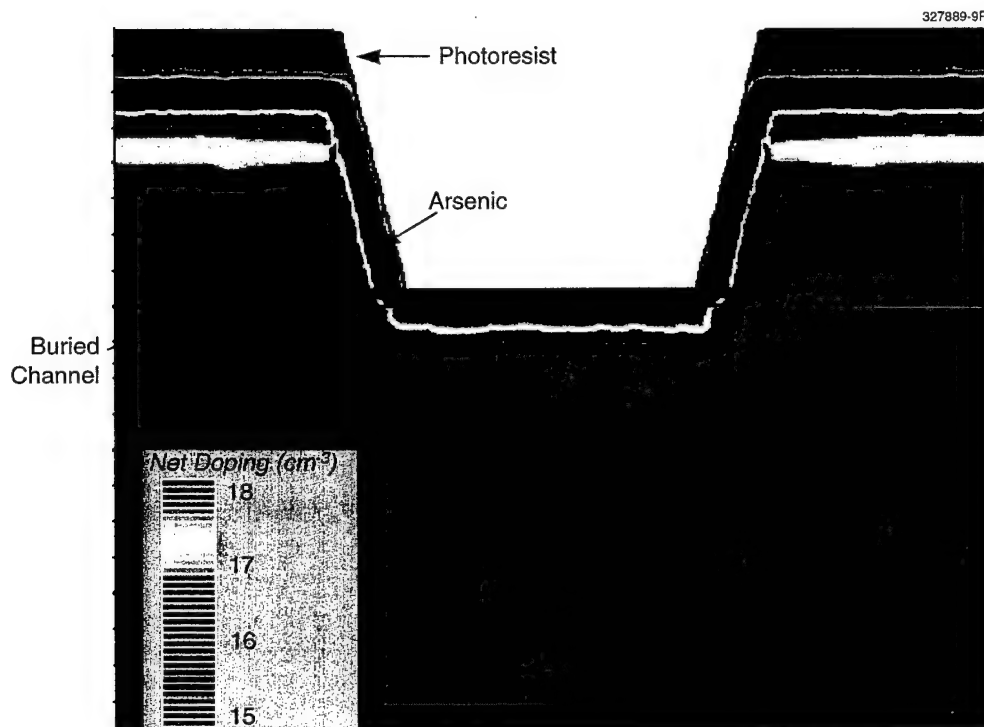
Figure 5-3. Results of simulation showing dopant distribution from three implant species with photoresist still in place on wafer. The color scheme reflects the net doping, $|N_D-N_A|$, with a range from 10^{15} to 10^{18} cm^{-3}.

27
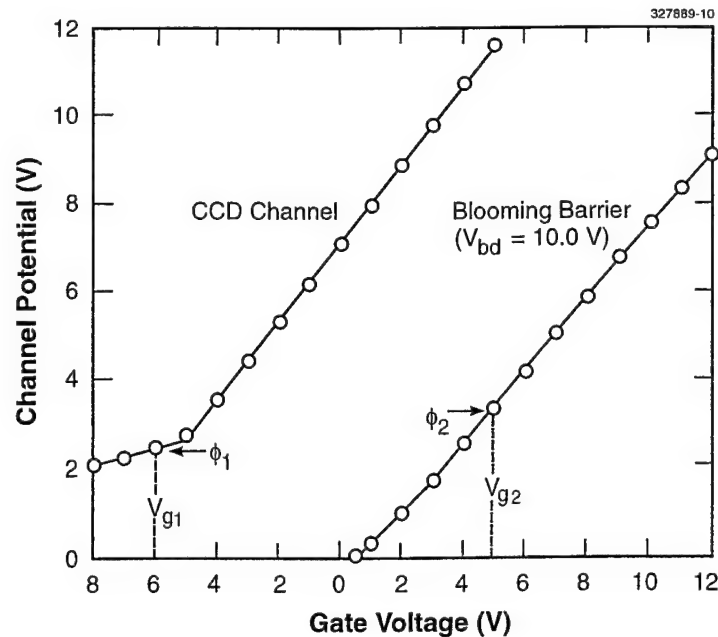
Figure 5-4. Potentials in charge-coupled device (CCD) channel and blooming barrier as a function of gate voltage obtained from test transistors next to CCD imager.

the barrier potential ϕ_2 under the collecting gate. This condition is satisfied by the clock settings illustrated in Figure 5-4, where the high and low clock phases are set to $V_{g1} = -6$ and $V_{g2} = +5$ V. If V_{g2} were lower than about 4 V, this condition would not be satisfied and charge could bloom into adjacent pixels.

Figure 5-5 illustrates the operation of the blooming control on a 512×512-pixel frame-transfer imager with 15-μm pixels. A light-emitting diode, located behind the handle of the cup, is pulsed on during image integration and produces a charge level of about 1000× well capacity. In Figure 5-5(a) the high level of the integration phase is set just below 4 V and severe blooming along the columns can be seen, while in Figure 5-5(b) it is set above this level and the blooming is suppressed. Additional tests have shown that the blooming control is effective even to overloads of 10^6×.

<div align="right">

B. E. Burke
J. A. Gregory
T. A. Lind

</div>

REFERENCE

1. E. D. Savoye, D. F. Battson, T. W. Edwards, W. N. Henry, D. R. Tshudy, L. F. Wallace, G. W. Hughes, W. F. Kosonocky, P. A. Levine, and F. V. Shallcross, *Proc. SPIE* **501**, 32 (1984).

327889-11P
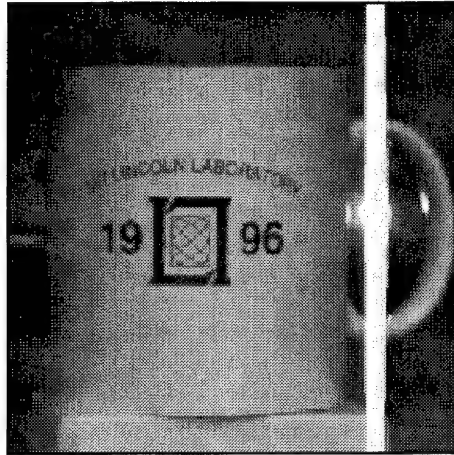
(a)

(b)

Figure 5-5. Images of coffee mug and bright light-emitting diode (LED) taken with blooming control (a) disabled and (b) enabled. The optical overload due to the LED is 1000×.

6. ANALOG DEVICE TECHNOLOGY

6.1 FIRST DEMONSTRATION OF CORRELATION IN A NIOBIUM SUPERCONDUCTIVE PROGRAMMABLE BINARY-ANALOG MATCHED FILTER

In past reports we described the architecture of the programmable filter for a superconductive direct-sequence spread-spectrum modem designed to operate at a chipping rate of 2 Gchips/s, and most recently we described the successful operation of the digital control registers at frequencies up to the full 2-GHz design speed with data patterns of the type that would be used during the operation of the filter [1]. We have now operated a complete preprototype filter using a seven-chip pseudonoise code sequence and have demonstrated correlation for the first time.

The modem's receiver channel requires a programmable matched filter (correlator) for establishing time synchronization between the receiver and the transmitter and for demodulating (despreading) the transmitted signal. A block diagram of the filter is shown in Figure 6-1. The filter includes identical sections, or slices, for each chip in the code pattern. Each slice is enclosed by a dashed box in Figure 6-1(a), and a more detailed block diagram of a slice that corresponds closely to the physical layout of the circuit is presented in Figure 6-1(b). The shaded areas indicate analog components, including track/hold (T/H) cells to capture samples of the received analog signal (the transmitted binary signal plus interference and noise) and nondestructive binary-analog tap weight units to multiply the analog signal samples by the binary reference code pattern. The upper part of each slice contains one stage of each of two binary shift registers and buffers to allow their signals to drive the associated analog components.

The bank of analog T/H cells (the analog data register) is controlled by the sampling control register, which is loaded with all 0's except for a single 1 (the index bit). The analog input signal is presented to all of the T/H cells, but only where the sampling control register contains a 1 does the corresponding T/H cell capture a new sample; the other cells continue to hold the sample they acquired previously. This 1 circulates through the shift register, causing successive analog samples to be taken in successive T/H cells. Thus, at any given time the most recent N samples of the input signal are stored in the analog data register, with the newest sample at the position of the index bit, with progressively older samples to the left and then wrapping around to the right, and with the oldest sample just to the right of the index bit. Note that the signal samples do not move through the analog data register. Rather, each sample remains in place for N clock cycles, at which point it is replaced by a newer sample.

The bank of tap-weight cells is controlled by the reference code register, which is loaded with a time-reversed copy of the code that was used in the transmitter to spread the signal. Each tap multiplies the analog sample stored in the corresponding T/H cell by either +1 or 0 (or, alternatively, +1 or −1) depending on the bit stored in the binary reference register. As the two shift registers are clocked synchronously, the reference code moves past the stationary analog samples of the input signal. When the reference code aligns with the received signal, a correlation peak occurs. The output signal peaks strongly in a positive direction for an encoded signal bit of 1 and in a negative direction for a signal bit of 0. The position in time
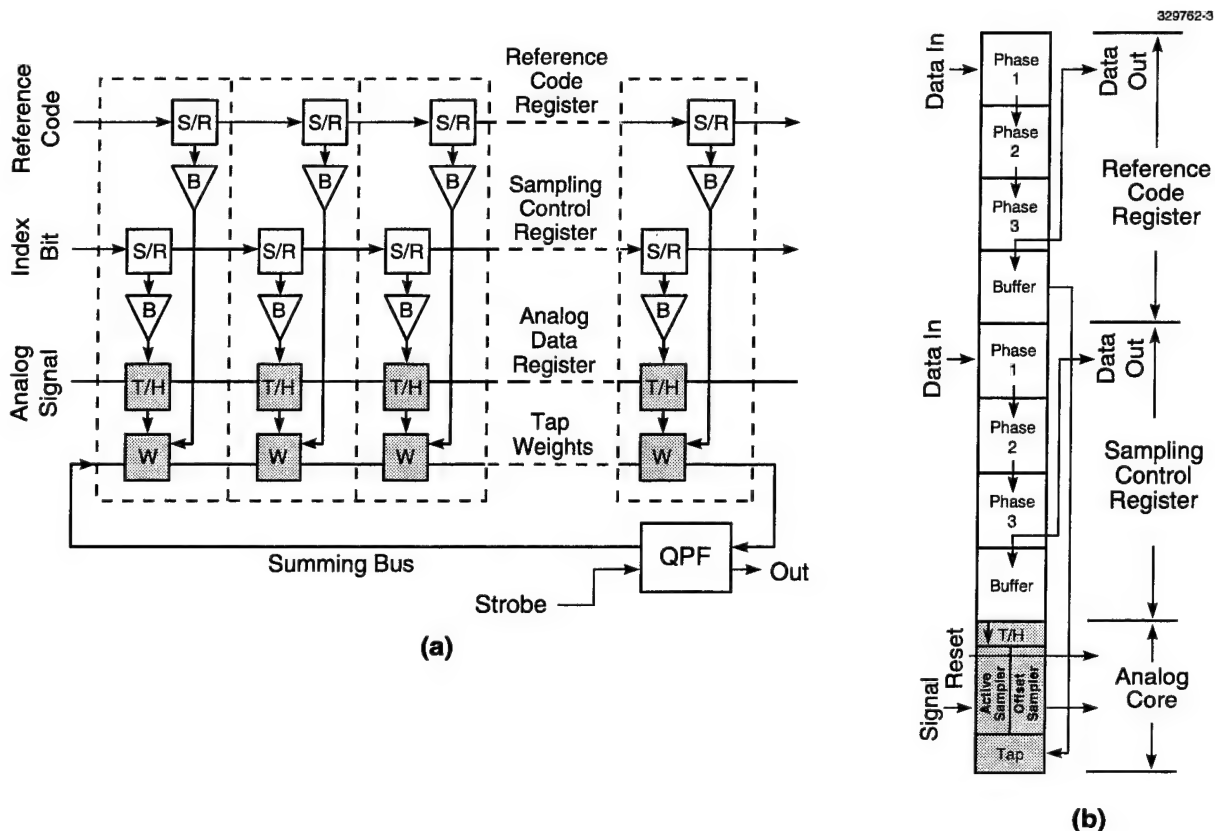
Figure 6-1. (a) Architecture of programmable matched filter that correlates received signal against prearranged reference code. The time position of the output provides the timing between the reference and the signal, while the positive or negative amplitude of the peak gives the value of the bit encoded in the signal. (b) Physical architecture of repeated building blocks, or slices, of filter. The shaded areas process analog signals.

of the correlation peaks provides synchronization information, while the polarity of each output peak provides the demodulated data bit. Note that in the course of operation, the signal stored in a T/H cell—which, as noted, changes only every N clock cycles—is multiplied by a sequence of varying reference bits. Consequently, the tap-weighting process must be nondestructive; that is, it must not alter the stored analog samples.

Figure 6-2(a) shows how the seven-chip preprototype filter is laid out physically. In order to minimize stray inductance in the summing bus, the slices are arranged in two banks, four above the summing bus and three below. The quantum flux parametron (QFP) output detector [2] occupies the free space on the shorter side. Figure 6-2(b) is a photograph showing most of an actual chip.

Slice 1

Slice 2

Slice 3

Slice 4

T/H | T/H | T/H | T/H

Tap | Tap | Tap | Tap

QFP Sense

Tap | Tap | Tap

T/H | T/H | T/H

Slice 7

Slice 6

Slice 5

(a)

327889-23P

(b)

Figure 6-2. (a) Block diagram of physical arrangement of components of seven-stage preprototype filter and (b) photograph of an actual chip. The photograph has been cropped slightly, so that the phase-1 latches of the reference code register are only partially visible in the top four slices and are not visible at all at the bottom three slices.

The entire seven-stage preprototype filter has been operated for the first time as a filter and has demonstrated matched-filter correlation using a seven-chip pseudonoise code sequence, thereby establishing the soundness of the design principles. Although we were able to show that the filter can perform the correlation function, two problems were encountered that forced us to perform the experiments at low speed using special experimental techniques. These were (1) a low signal amplitude in the summing bus as a result of higher-than-expected parasitic inductances in the tap circuit, and (2) a high level of direct feedthrough to the summing bus from other parts of the circuit. We believe that the feedthrough is associated with magnetic fields generated by return currents in the ground plane, but we have not succeeded in finding a detailed model for the phenomenon.

The very small signal levels in the summing bus were measured with great precision by operating the QFP sense circuit in a special way [3]. The QFP has two inputs, one from the summing bus and one from an external signal. Normally, that external signal would set the detection threshold for individual measurements of the filter output. Instead, we cycled the QFP many times for each measurement while adjusting the external signal to maintain the QFP right at its threshold point (where it switches 50% of the time into each of its two states). This procedure was found to give repeatable results with a sensitivity of about 0.07 μA of current in the summing bus.

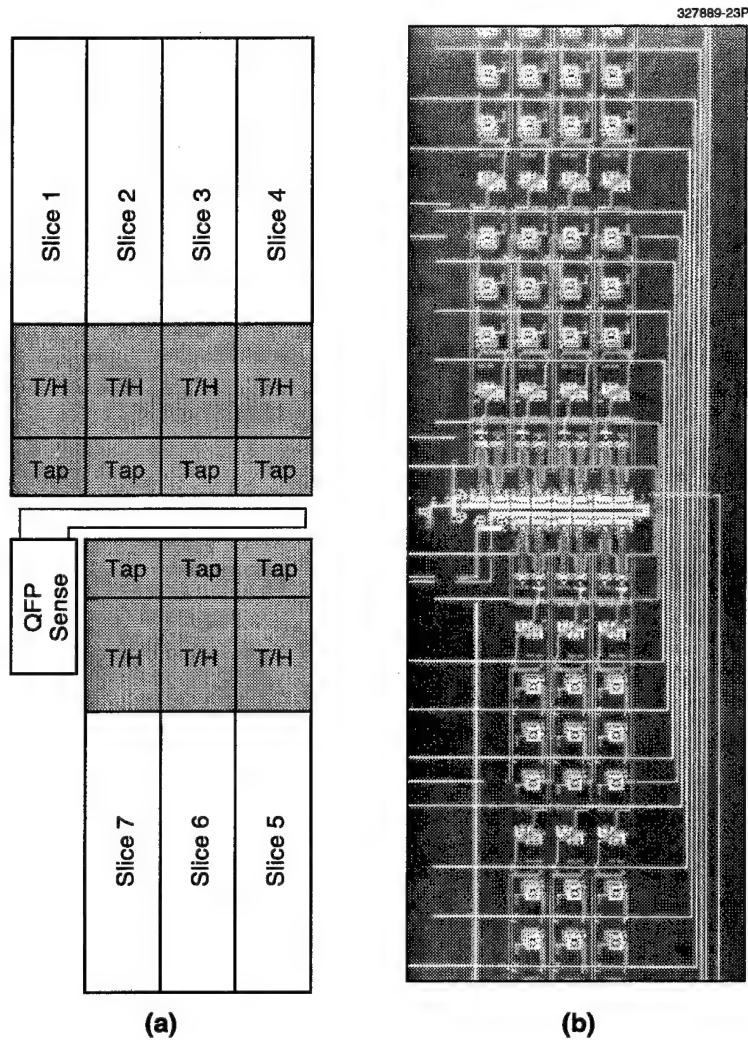The sensitivity with which the filter response could be measured was further enhanced by varying the input signal amplitude over its full bipolar dynamic range and taking the slope of a straight-line fit between the input signal and the summing bus response. This technique also eliminates any effect of direct feedthrough from non-signal-dependent sources, such as the currents in the shift registers and buffers. To eliminate feedthrough from the signal line itself, a set of analog samples was captured in the analog data register and then the signal was brought to zero before the correlator output was measured.

Since the operation of the complete filter is a complex process, we approached it step by step, verifying sequentially that each piece of the chip was working. To avoid the feedthrough problem, wherever possible we used waveforms that could be pulsed and then removed while the output was detected. For example, the first check was that the buffers between the sampling control register and the T/H cells were operating properly and had enough output to drive the active sampler. In this case we raised the input analog signal to the desired value and then pulsed the clock line to the buffers to a level above the normal operating point, to force them to switch momentarily to the voltage state even without inputs from the sampling control register. This should latch the signal level into all seven T/H cells. The analog signal was then removed, eliminating all sources of feedthrough. At that point the QFP was exercised as described earlier. Thus the average responsivity of the seven slices with tap weights of 1 was measured.

The next step was to test the operation of the taps. By applying a sufficiently high dc current to the clock line that biases the buffers on the outputs from the reference code register, all the taps can be made to switch to and remain in the 0 state. As above, the average responsivity of the seven slices was measured. In fact, we found that the tap weight in the nominal 0 state is not zero but rather approximately 0.4. Some of the leakage undoubtedly results from feedthrough from the currents stored in the T/H cells to the summing bus, but we believe that the tap circuit itself also has some parasitic inductive coupling directly between its input and output windings.

The next experiments were designed to check the operation of the shift registers. Output lines from the registers verified that binary data was passing through them; the only remaining question was whether the shift register outputs would trigger the buffers (in the previously described experiments the buffer clock was driven to a high enough level that the buffers fired without any input from the shift registers). In one experiment, a pattern with a single 1 was loaded into the sampling control register, and then the buffer clock was pulsed to its normal operating level (so that it will fire only when there is an input from the associated shift register) to store a signal into just the single selected T/H cell. The slope of the output as the signal amplitude was varied is shown in Table 6-1 for each of the seven slices. This experiment established that the analog registers in all seven slices were working and had nearly equal gain (though the three slices below the summing bus appear to have a slighly higher gain). A similar experiment was performed with the reference code register to verify that each tap could be addressed.

For the final experiment to demonstrate full filter operation, the pseudonoise code sequence 1110100 was used. A unipolar input signal with amplitude A for the 1's and zero for the 0's was applied while a single 1 was propagated through the sampling control register. This loaded the signal pattern into the array of T/H cells. Concurrently, the time-reversed pattern 0010111 and its time-shifted versions (1001011, 1100101, etc.) were loaded into the reference code register. For each reference pattern the filter output was then measured as described earlier over the full bipolar dynamic range of signal amplitude A. The responsivity of the filter (change in output per unit change of input) is plotted in Figure 6-3 as a function of the number of chips by which the reference code was rotated from alignment with the input signal.

TABLE 6-1
Variation of Sensitivity from Slice to Slice

Sampling Control Register Pattern	Responsivity of Selected Slice
1000000	0.0032 ± 0.0005
0100000	0.0032 ± 0.0001
0010000	0.0033 ± 0.0002
0001000	0.0033 ± 0.0002
0000100	0.0037 ± 0.0006
0000010	0.0035 ± 0.0005
0000001	0.0038 ± 0.0001

35

327989-24
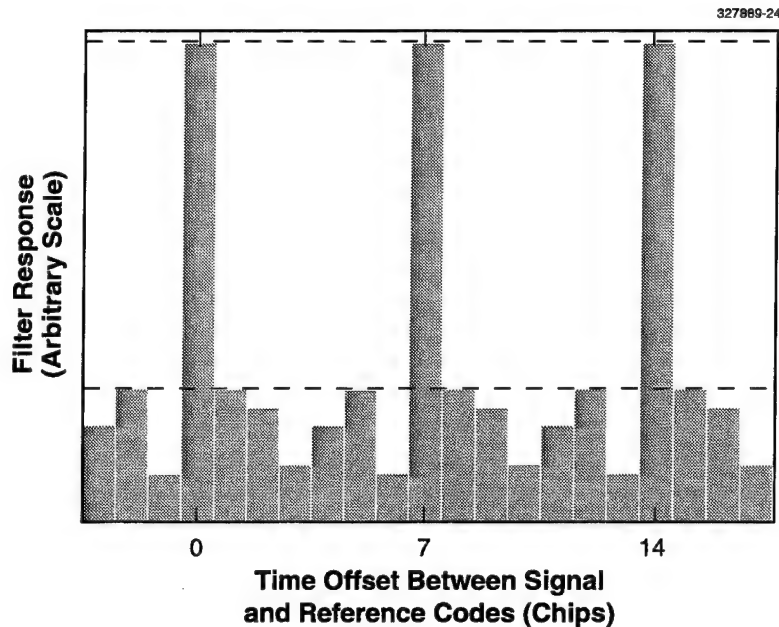
Figure 6-3. Relative output from matched filter when the reference pattern was a seven-chip pseudonoise sequence and the signal pattern was a repeated waveform of the same pseudonoise sequence. The dashed horizontal lines indicate the peak and sidelobe response levels predicted from the measured sensitivity of slices.

From the average per-slice responsivity the expected peak and sidelobe responses of the filter could be estimated. For the peak response, all four slices where a signal is present line up with tap weights of 1 to give a response of 4.0 times that of a single slice with weight 1. For the sidelobes, two of the slices with a signal present line up with weights of 1, while the other two line up with nominal weights of 0. For a 0-weight tap response of about 0.4, the sidelobe response would, thus, be $(2 \times 1.0) + (2 \times 0.4) = 2.8$ times that of a single slice. Those levels are indicated by dashed lines in Figure 6-3. The peaks agree exactly, while the sidelobes all fall below the expected level, presumably because we overestimated the tap leakage.

To conclude, in the past we had demonstrated the functionality of each individual element of a super-conductive programmable binary-analog matched filter for a 2-Gchip/s direct-sequence spread-spectrum modem. Now all of those elements have been operated together in a complete preprototype filter in low-frequency tests. The filter produced the correct output for a seven-chip pseudonoise code sequence. Two significant problem areas were identified: low signal levels aggravated by larger-than-expected parasitic inductance effects and direct feedthrough of clock and control currents to the filter output.

J. P. Sage
K. K. Berggren
D. A. Feld

REFERENCES

1. Solid State Research Report, Lincoln Laboratory, MIT, 1997:2, p. 31.

2. Solid State Research Report, Lincoln Laboratory, MIT, 1994:4, p. 33.

3. D. A. Feld, J. P. Sage, K. K. Berggren, and A. Siddiqui, to be published in *IEEE Trans. Appl. Supercond.*

7. ADVANCED SILICON TECHNOLOGY

7.1 PATTERN ASYMMETRIES IN PHASE-EDGE IMAGING

Strong phase-shift methods such as alternating aperture and chromeless edge are resolution-enhancement techniques (RETs) that promise to extend optical lithography to the 100-nm regime and possibly below [1]. Figure 7-1 is an example of the imaging obtainable using strong phase shifting [2]. Semi-isolated polysilicon features of 60-nm critical dimension (CD) were fabricated using a 248-nm stepper. In order to help evaluate the practical application of this RET to circuit fabrication, it is important to understand the origin of asymmetries that can occur with such imaging techniques. Two experimentally observed asymmetries will be explored involving linewidth and pitch. The origin of these effects will be investigated by careful study of the phase-shift mask as well as consideration of lens aberrations. The former is of interest for the developing mask-making and metrology infrastructure. The latter is important because aberration effects can have widely differing magnitudes depending on the type of RET used [3]–[6]. An understanding of these asymmetry effects is crucial for the practical implementation of strong phase-shift RETs because of the requirements of tight CD control and pattern placement over the full field.

327889-25P
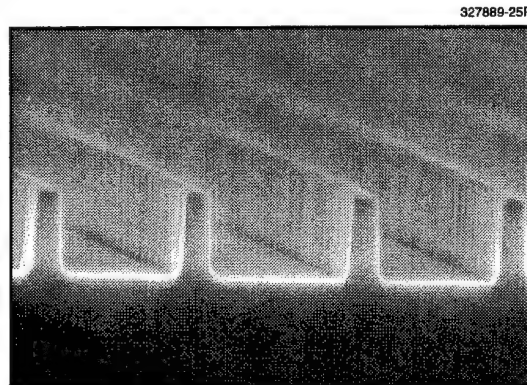
Figure 7-1. Scanning electron micrograph (SEM) of polysilicon grating imaged with chromeless phase-edge reticle and 0.48-numerical-aperture (NA) 248-nm stepper. The critical dimension (CD) is 60 nm and the pitch is 350 nm.

Our work makes use of a GCA XLS 248-nm DUV 4× stepper with numerical aperture (NA) = 0.48 and adjustable sigma. We fabricated our own chromeless masks by reactive ion etching a standard chrome-on-quartz mask followed by a wet chrome-strip etch. Most of the results obtained here are just as valid for alternating-aperture masks which are more commonly used in applications. Most of the phase-shift patterns we consider are in the range 50–150 nm and were exposed with a partial coherence σ = 0.3. Simulation work was carried out using PROLITH/2 Version 5.0 by FINLE Technologies.

The first type of asymmetry we consider is the critical dimension (CD) asymmetry observed between the left and right edges of a phase-edge pattern. Figure 7-2 shows two scanning electron micrographs (SEMs) of this effect in cross section and top down. Asymmetric phase-edge patterns have been attributed to differences in the edge profile of the chromeless etch so it is important to investigate the mask [7],[8]. Figure 7-3 is a cross-sectional SEM view of a chromeless test mask fabricated in the same way as the one we employed in this work. Note the sidewalls are nearly 90° and there is no evidence of asymmetry in the etched glass sidewall profiles. There is, however, a noticeable line to space asymmetry which will be discussed. The etch depth is also well controlled to the desired $\lambda/2(n-1)$ value of 2440 Å. It has been shown that shifter edge angles must drop to the 60° range before significant linewidth asymmetries show up [8].

(a)   (b)
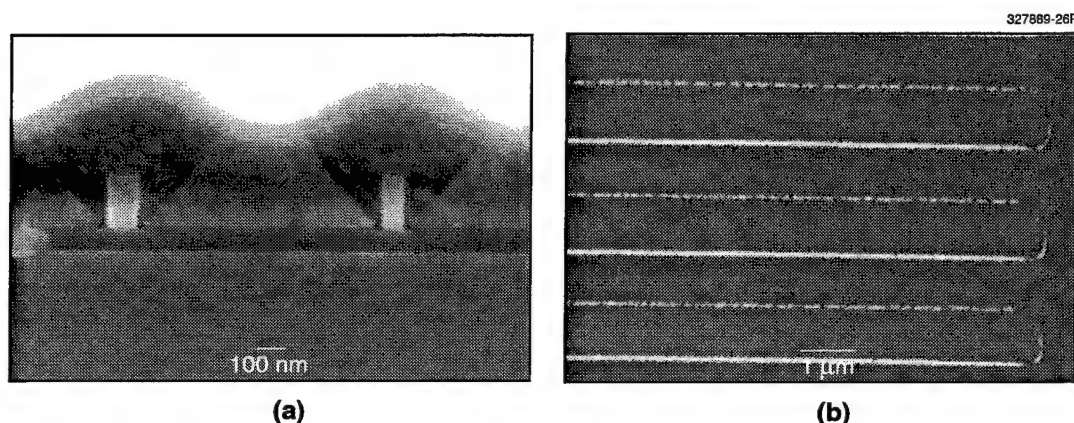
Figure 7-2. SEMs of left-right CD asymmetry in polysilicon: (a) cross-sectional and (b) top-down views. In (a) the poly lines were coated with SiO_2 before cleaving. In (b) the alternating lines are well and poorly resolved.
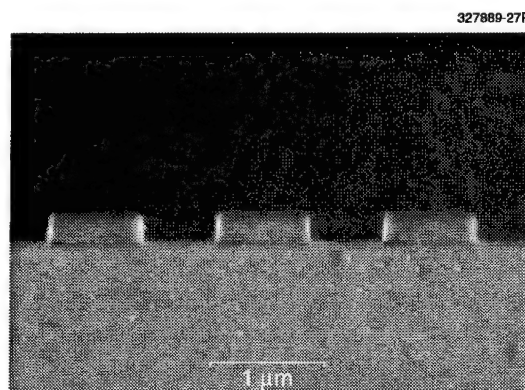

Figure 7-3. Cross-sectional SEM of chromeless phase-edge reticle. Note the symmetric, nearly vertical sidewall profile and the line to space asymmetry of 1.5 to 1. The stepper reduction factor is 4×.

40

Thus we must look elsewhere to explain the effects we have observed in Figure 7-2. The precise control of the etch depth and profile will be challenges to the phase-shift mask-making and metrology infrastructure, but our results suggest that this should be achievable.

We now turn to studying the effects of lens aberrations on chromeless phase-edge imaging. Lens aberrations cause wavefront deviations across the lens pupil that are typically expressed as a Zernike polynomial series [9],[10],

$$\text{OPD}(\rho,\varphi) = \sum a_j \lambda Z_j(\rho,\varphi) \tag{7.1}$$

where the optical path difference (OPD) is expressed in cylindrical coordinates ρ and φ in the pupil plane. The lower-order terms represent the common aberrations faced in lithography: tilt, defocus, astigmatism, coma, and spherical. Defocus and third-order spherical are symmetric aberrations and thus cannot lead to edge asymmetry. Tilt leads to a simple linear shift in the pattern position. Astigmatism is asymmetric and is typically observed as a focus shift between horizontal and vertical lines in the x-y coordinate system common for circuit patterns. This aberration does not lead to pattern edge asymmetries. The only low-order Zernike term that can yield pattern edge asymmetries is coma [8]–[10], so we will explore the effect of this term on phase-edge imaging.

Figure 7-4 is a PROLITH plot of OPD surfaces for two types of aberration described by the tilt and x-coma Zernike terms. Tilt is a simple linear displacement of the OPD surface. In coma aberration, the wavefront shift depends on the pupil radius in an asymmetric way and also changes sign depending on the pupil position of the imaging ray [9],[10]. This can be viewed as a variation of magnification with aperture. Coma gives rise to pattern-dependent image shifts and pattern asymmetry. Coma-induced image shifts can have significant effects on device fabrication [11] owing to the stringent overlay requirements of today's design rules. In this work, we will focus on the linewidth asymmetry effects produced by coma.

When analyzing the effects of aberration on imaging performance, it is useful to look at the frequency-space representation of the problem [9],[12],[13]. The image pupil of a stepper is located at the Fourier-transform plane of the optical system. The mask pattern is Fourier transformed by the imaging system with a frequency distribution in the pupil plane determined by the pattern type. Comparison of the image frequency distribution with the shape of the OPD surface gives insight into the importance of a given aberration term for a given pattern shape. The use of RETs leads to specific types of frequency distributions which can degrade or improve imaging performance depending on the type of aberration considered [3]–[6]. In our simulation work, we considered two common circuit patterns with distinctive Fourier transforms: a phase-edge grating and a single phase-edge pair. The former is used in contact array applications, and the latter in isolated gate pairs common in inverter elements. Figure 7-5 is a plot of the Fourier transforms of these two pattern types using PROLITH. Note that the single phase-edge pair has its intensity maximum at the pupil center and numerous sidelobes, while the grating has only two diffraction orders with no sidelobes and a separation determined by the grating pitch. This type of frequency behavior

41

(a)   **(b)**
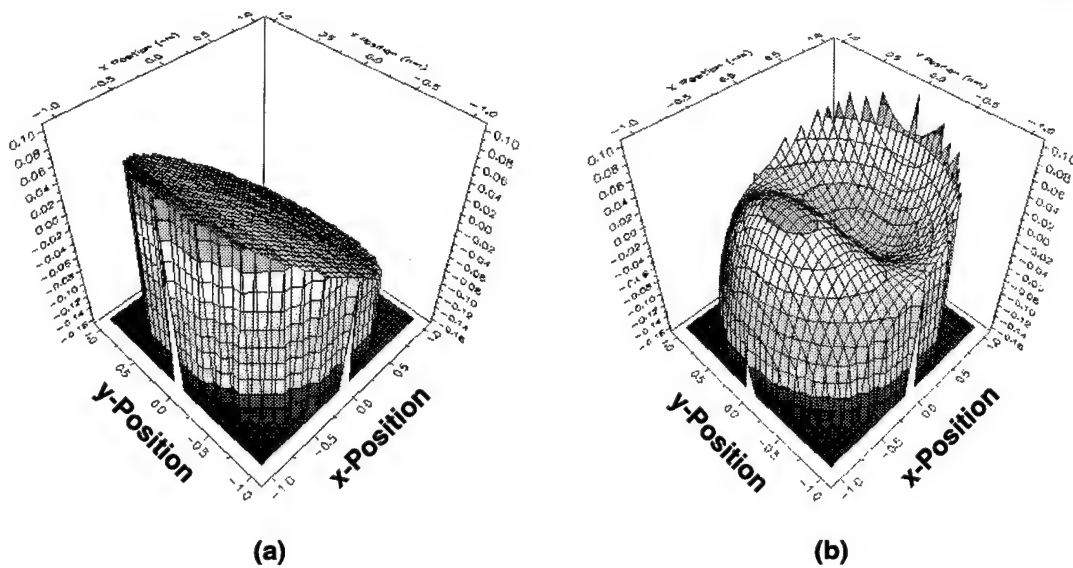
Figure 7-4. Calculated optical path difference (OPD) surfaces for (a) x-tilt, and (b) x-coma aberrations, each of magnitude 0.1 wavelength. The z-axis is in waves and the x-y axes are in relative pupil plane coordinates.

(a)   **(b)**
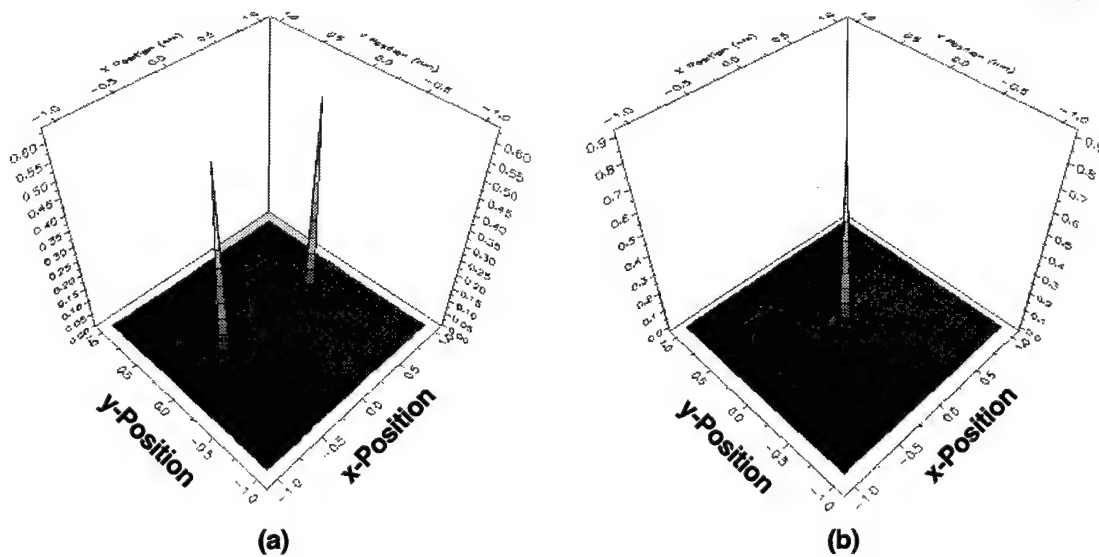
Figure 7-5. Calculated Fourier spectra for (a) 0.5-μm phase-edge grating and (b) 0.5-μm pitch phase-edge pair. The z-axis is in magnitude while the x-y axes are in relative pupil plane coordinates.

is typical for phase-edge mask patterns [13]. Note that the plotted Fourier transforms are for zero partial coherence with the peaks broadening in proportion to increasing σ. The effect of coma on these patterns will be strongly dependent on the Fourier-transform frequency distribution. Partial coherence will also play an important role as it determines how much the pupil aberrations are "averaged" out. Thus it is difficult to judge coma effects by simply looking at a single pattern type or σ value.

Figure 7-6 is a plot of the resist profiles obtained from a 0.5-μm phase-edge pair in the presence of 0.1 waves of coma. We used our known stepper and resist parameters for this simulation. Note the distinct linewidth asymmetry evident here. The printed lines have also undergone a *shift* from the symmetrical mask positions of ±250 nm. The effects of coma on this type of phase-edge pair are summarized in Figure 7-7(a). Note how the left-hand CD is hardly affected while the right-hand edge has large CD variations
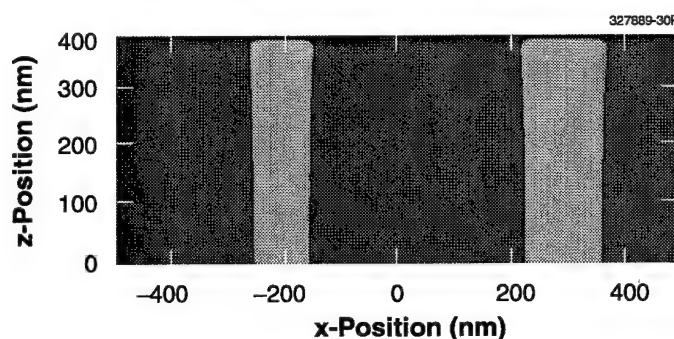
Figure 7-6. Simulated resist profile for 0.5-μm phase-edge pair with 0.1 waves of x-coma. The stepper NA = 0.48 and σ = 0.3.
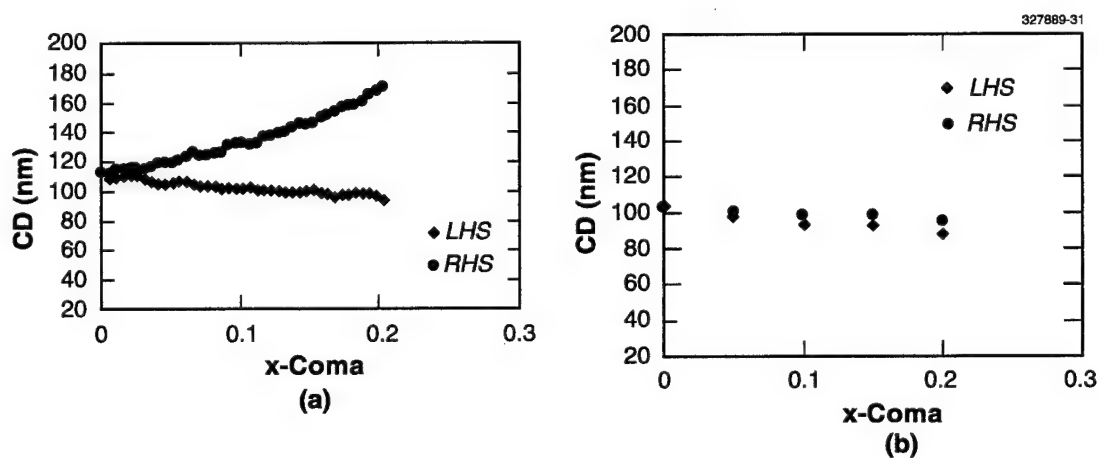
Figure 7-7. Simulations of coma effects on resist CD. Results are shown for (a) 0.5-μm phase-edge pair and (b) 0.5-μm phase-edge grating.

43

with increasing coma. Figure 7-7(b) is the same plot for a phase-edge grating of the same pitch. Note how coma has much less effect in this case. This is explained by the different frequency distributions of these two patterns. It should be kept in mind that the image *shift* is significant for both patterns, about 50 nm for 0.1 waves of coma. Figure 7-8 summarizes the effect of partial coherence on image asymmetry, for 0.1 waves of coma. It can be seen from this plot that the amount of asymmetry is somewhat dependent on sigma. This occurs because the part of the OPD surface covered by the pattern's Fourier components depends on sigma. Figure 7-9 summarizes the pitch dependence of coma aberration. Note how coma-induced CD asymmetry increases with decreasing pitch. Once again, this effect is less important for the phase-edge grating.
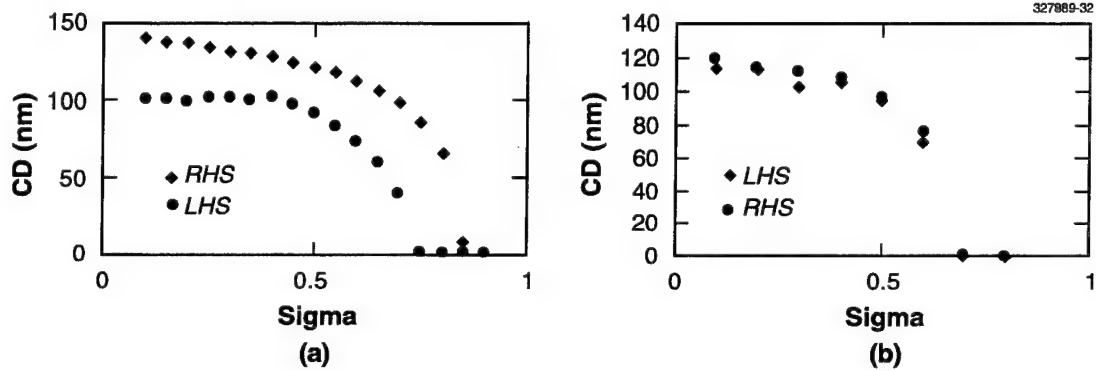
Figure 7-8. Simulated partial coherence dependence of coma aberration effect for (a) phase-edge pair and (b) phase-edge grating.
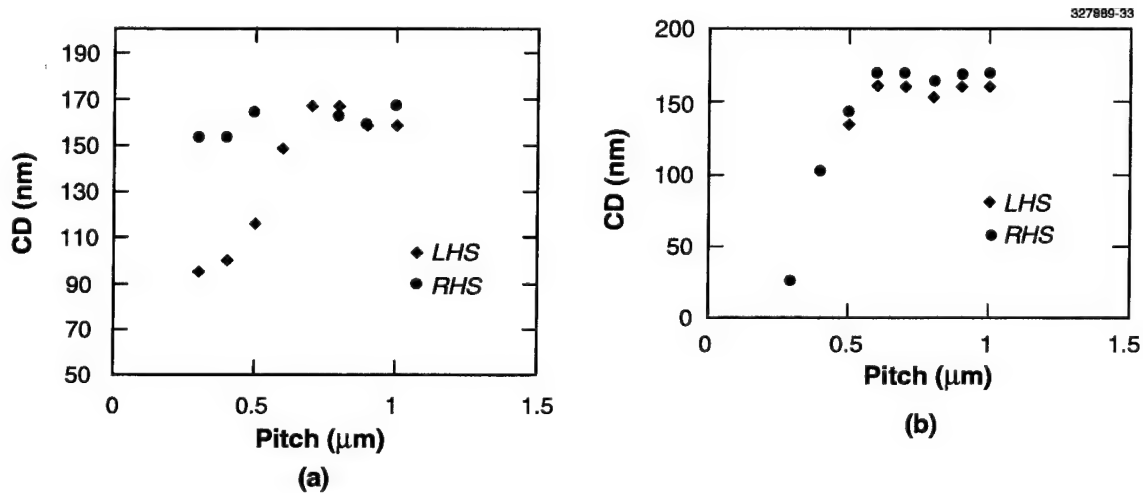
Figure 7-9. Simulated pitch dependence of coma effects for (a) phase-edge pair and (b) phase-edge grating.

44

Figure 7-10 shows the experimental effect of two Zernike aberrations on a phase-edge pattern. In this image, the dark lines are phase-edge lines printed in resist. The difference in resolution for horizontal and vertical lines is evidence of astigmatism while the left-right asymmetry of the horizontal lines indicates coma may be present. However, this is not a complete explanation because our simulations have shown that coma-induced CD asymmetry is quite small for the large pitch values involved here. This discrepancy needs to be understood. Careful investigation of our stepper focus performance revealed a significant lens *tilt* effect. When this tilt was corrected, by adjusting the lens, the CD asymmetry at large pitch was eliminated, as shown in Figure 7-11. It seems that coma and tilt effects are related in some way. This relationship needs to be quantified. Figure 7-12 shows two OPD surfaces for 0.1 waves of x-coma combined with (a) positive and (b) negative x-tilt. It is clear from these plots that tilt can act to increase coma effects or moderate them depending on the sign. This explains how dealing with the lens tilt solved our problem of CD asymmetry in Figure 7-10. In fact, adjusting the tilt has been proposed as a method of moderating other coma-induced effects such as pattern shifting [3]. Pattern-shifting effects can also be caused by other stepper-related effects such as condenser tilt [14].

The other asymmetry we will consider involves pitch. Figure 7-13 shows two scanning electron micrographs of phase-edge gratings as a function of pitch. Note the distinct alternating pitch asymmetry, which grows worse as the average pitch is decreased. We have typically observed this trend for phase-edge gratings with decreasing pitch. Such behavior has been attributed to asymmetric etch profiles in chromeless masks [7]. Consideration of the mask profile in Figure 7-3 shows that this is not a likely cause in our case where symmetric, nearly vertical sidewalls were observed.
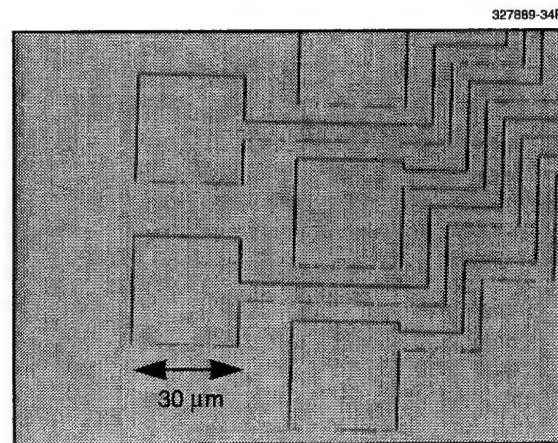
Figure 7-10. Top-down confocal microscrope view of phase-edge left-right asymmetries observed at large pitch values. The narrow resist lines appear dark in this image. Note the asymmetry in the horizontal lines with the upper ones well resolved and the lower ones only partly resolved.

45
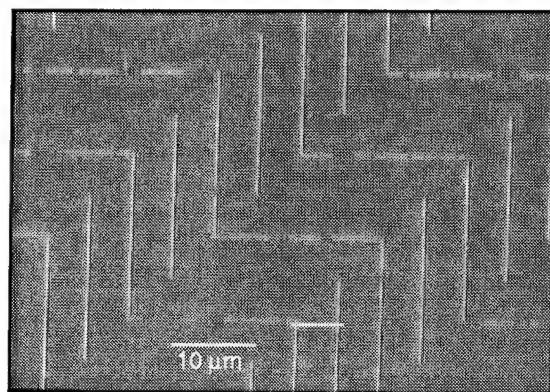
(a)
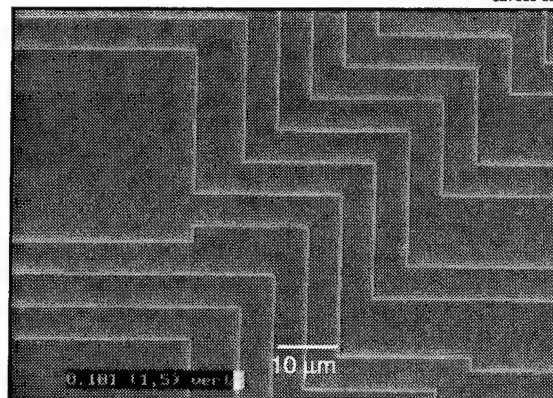
(b)

Figure 7-11. Top-down SEMs of phase-edge left-right asymmetries (a) in the presence of significant lens tilt and (b) with the lens tilt corrected. In these images the narrow resist lines appear bright.
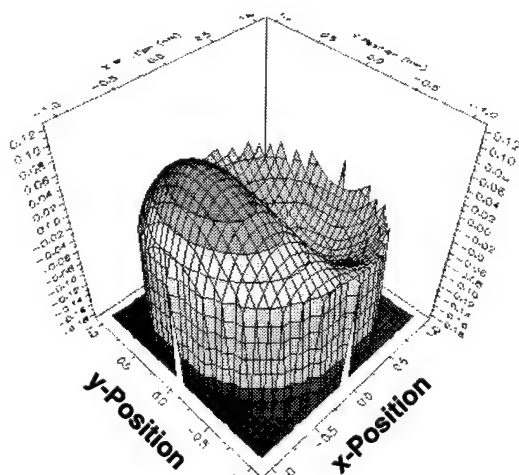
(a)
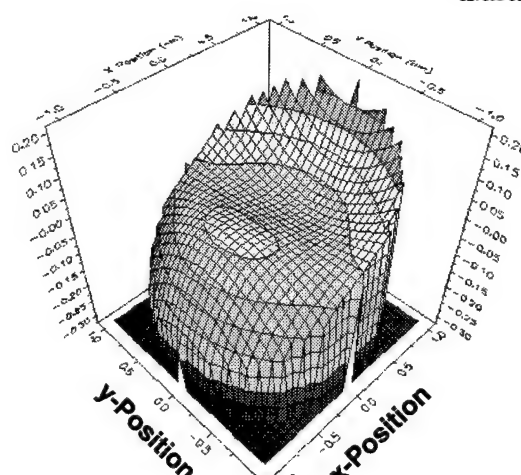
(b)

Figure 7-12. Simulated OPD surfaces for combined coma and tilt aberrations: (a) x-tilt = +0.1 and x-coma = 0.1 waves, and (b) x-tilt = –0.1 and x-coma = 0.1 waves.
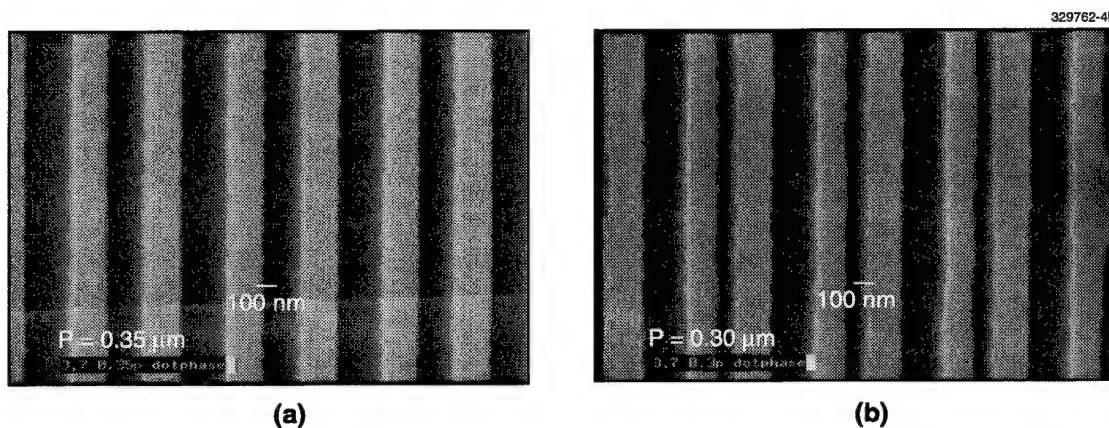
Figure 7-13. SEMs of pitch asymmetries in etched polysilicon observed at (a) 0.35-µm and (b) 0.30-µm average pitch values. The pitch asymmetries are 1/1.2 and 1/1.7, respectively.

Another mask-related effect that can cause alternating pitch asymmetry is a difference in transmission between the two phases of a chromeless grating. This might come about, for example, by etch damage to the glass causing lowering of the transmission in the etched regions. Figure 7-14 shows the results of a PROLITH simulation we have run to explore this effect. Here we plot pitch vs the transmission of the etched phase in a quartz grating of 0.5-µm lines and spaces. Following the convention of this work, all dimensions discussed are in wafer units with the exception of the reticle data in Figures 7-3 and 7-15. We can see that there is no significant pitch asymmetry until the transmission of the etched phases drops below 75%. This seems to indicate that this effect is unlikely to explain our observations, but careful transmission study of etched fused silica is necessary in the fabrication of these masks. We note that we have observed no difference in the dose to clear for the etched vs the unetched portions of our mask.

We now turn to a consideration of the mask line to space ratio. Figure 7-15 shows a top-down atomic force microscope view of a nominally equal line and space grating on our chromeless mask. Careful inspection of this plot reveals an asymmetry in the line to space ratio of about 1.5 to 1. This is unlikely to be caused by our mask etch process because of the excellent profiles observed in Figure 7-3. We suspect that this asymmetry may be coming from the original chrome mask pattern we used to generate our chromeless masks. Figure 7-16 plots the measured CD vs the desired CD for dense and isolated patterns on one of our typical chrome masks (the axes are in wafer units). Note the deviation from the desired values for dense lines, which is worse for decreasing pitch. We thus conclude that much of the pitch asymmetry apparent in Figure 7-13 results from mask errors. This observation highlights a major concern regarding the mask-making effort, namely, the e-beam proximity effects which are not obvious to the user when mask qualification is performed at only one CD value.

47
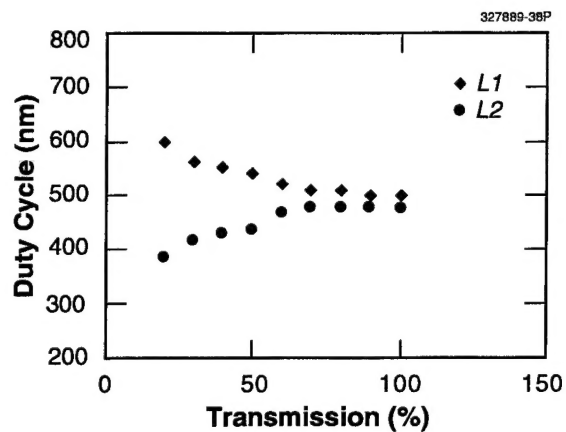
Figure 7-14. Simulation result for pitch asymmetry vs transmission factor of etched phase in chromeless phase-edge mask with average pitch of 500 nm.
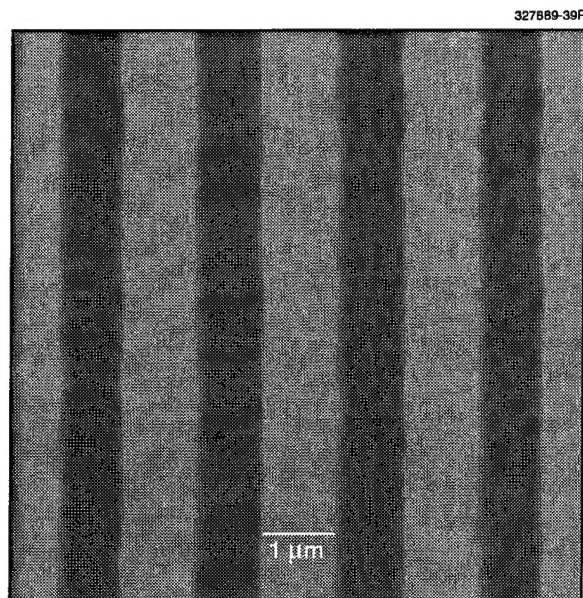
Figure 7-15. Top-down atomic force microscopy trace of one of our chromeless reticles. Note the line to space asymmetry of 1.0(line)/0.8(space).

48
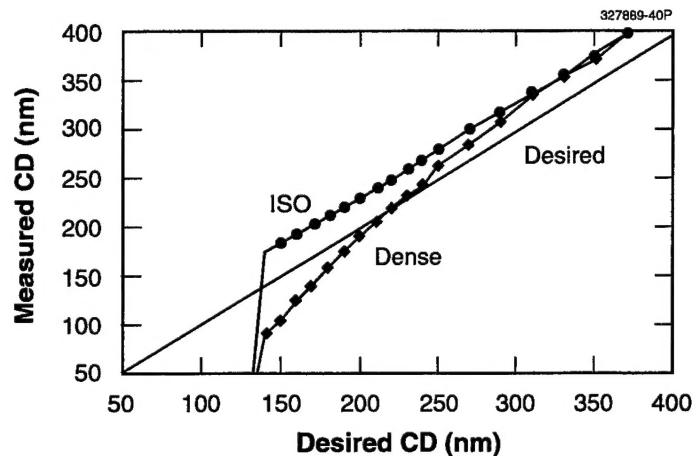
Figure 7-16. Experimental plot of measured vs desired CD for one of our typical chrome reticles used in fabrication of chromeless reticles. Note how the mask error becomes worse with decreasing CD for the dense lines. The dimensions are in wafer units.

We have also observed that this alternating pitch asymmetry tended to be larger at the lens field edges. This argues that lens aberration may be adding to the mask errors discussed above. The effects of optically induced mask error magnification have recently been reported [15]. In this work, it is shown that mask errors can be magnified and that this effect is particularly large for small pitch values. (Small here means pitch values approaching the Rayleigh resolution limit of 0.5λ/NA.) In this regime, mask errors can be nonlinearly magnified with mask error factors quickly exceeding 2.0. The problem of mask error magnification will be a challenge for future mask-making and metrology efforts below the 0.18-μm design rules.

M. Fritze
S. Cann
P. Wyatt

REFERENCES

1. M. D. Levenson, *Proc. SPIE* **3051**, 1 (1997); T. Brunner, *International Electron Devices Meeting Technical Digest* (IEEE, Piscataway, N.J., 1997), p. 9.

2. M. Fritze, D. Astolfi, H. Liu, C. K. Chen, V. Suntharalingam, D. Preble, and P. W. Wyatt, to be published in *J. Vac. Sci. Technol. B* **17** (March/April 1999).

3. B. Smith and J. S. Peterson, *J. Vac. Sci. Technol. B* **16**, 3405 (1998).

4. R. L. Kostelak, E. L. Raab, and S. Vaida, *J. Vac. Sci. Technol. B* **12**, 3793 (1994).

5. A. Kroyan, M. D. Levenson, and F. K. Tittel, *Proc. SPIE* **3334**, 832 (1998).

6. K. Tsujita, J. Sakai, A. Nakae, S. Nakao, and W. Wakamiya, *Proc. SPIE* **3334**, 855 (1998).

7. K. H. Toh, G. Dao, R. Singh, and H. Gaw, *Proc. SPIE* **1463**, 74 (1991).

8. M. Nakatani, Y. Kojima, H. Nakano, K. Kamon, K. Sato, H. Takano, and O. Ishihara, *Jpn. J. Appl. Phys.* **34**, 5043 (1995); M. Nakatani, H. Matsuoka, H. Nakano, K. Kamon, K. Sato, O. Ishihara, and S. Mitsui, *Proc. SPIE* **2197**, 158 (1994).

9. C. A. Mack, in *Microlithography: Science and Technology*, J. R. Sheats and B. W. Smith, eds. (Marcel Dekker, New York, 1998), p. 118.

10. T. A. Brunner, *Proceedings of OLIN Interface Microlithography Conference* (OLIN, Norwalk, Conn., 1996), p. 1.

11. M. Chan, R. R. Kunz, S. P. Doran, and M. Rothschild, *J. Vac. Sci. Technol. B* **15**, 2404 (1997).

12. E. G. Steward, *Fourier Optics: An Introduction,* 2nd ed. (Ellis Horwood, Chichester, England, 1987), Chap. 5.

13. K. Ronse, M. Op de Beeck, L. Van den Hove, and J. Engelen, *J. Vac. Sci. Technol. B* **12**, 589 (1994).

14. T. Terasawa, N. Hasegawa, S. Katagiri, and K. Hama, *Proc. SPIE* **1674**, 127 (1992).

15. J. Randall and A. Tritchkov, *J. Vac. Sci. Technol. B* **16**, 3606 (1998).

REPORT DOCUMENTATION PAGE

1. AGENCY USE ONLY (*Leave blank*)	2. REPORT DATE 15 February 1999	3. REPORT TYPE AND DATES COVERED Quarterly Technical Report, 1 November 1998–31 January 1999

4. TITLE AND SUBTITLE

Solid State Research

5. FUNDING NUMBERS

C — F19628-95-C-0002

6. AUTHOR(S)

David C. Shaver

7. PERFORMING ORGANIZATION NAME(S) AND ADDRESS(ES)

Lincoln Laboratory, MIT
244 Wood Street
Lexington, MA 02420-9108

8. PERFORMING ORGANIZATION REPORT NUMBER

1999:1

9. SPONSORING/MONITORING AGENCY NAME(S) AND ADDRESS(ES)

HQ Air Force Materiel Command
AFMC/STSC
Wright-Patterson AFB, OH 45433-5001

10. SPONSORING/MONITORING AGENCY REPORT NUMBER

ESC-TR-98-055

11. SUPPLEMENTARY NOTES

None

12a. DISTRIBUTION/AVAILABILITY STATEMENT

Approved for public release; distribution is unlimited.

12b. DISTRIBUTION CODE

13. ABSTRACT (*Maximum 200 words*)

This report covers in detail the research work of the Solid State Division at Lincoln Laboratory for the period 1 November 1998–31 January 1999. The topics covered are Quantum Electronics, Electro-optical Materials and Devices, Submicrometer Technology, Biosensor and Molecular Technologies, Microelectronics, Analog Device Technology, and Advanced Silicon Technology. Funding is provided by several DoD organizations — including the Air Force, Army, BMDO, DARPA, Navy, NSA, and OSD — and also by the DOE, NASA, and NIST.

14. SUBJECT TERMS

quantum electronics	biosensor technology	microchip lasers	bioelectronic sensors
electro-optical devices	microelectronics	mass-transported microlenses	charge-coupled device imagers
materials research	analog device technology	microlithography	programmable filters
submicrometer technology	advanced silicon technology	electrochemical detection	phase-edge imaging

15. NUMBER OF PAGES
72

16. PRICE CODE

17. SECURITY CLASSIFICATION OF REPORT	18. SECURITY CLASSIFICATION OF THIS PAGE	19. SECURITY CLASSIFICATION OF ABSTRACT	20. LIMITATION OF ABSTRACT
Unclassified	Same as Report	Same as Report	Same as Report